The Astrophysical Journal, 944:144 (18pp), 2023 February 20 https://doi.org/10.3847/1538-4357/acaf56


# The Influence of $\beta$-decay Rates on *r*-process Observables

Kelsey A. Lund[1,2,3], J. Engel[4], G. C. McLaughlin[1,3], M. R. Mumpower[2,3,5], E. M. Ney[4], and R. Surman[3,6]
[1] Department of Physics, North Carolina State University, Raleigh, NC 27695, USA; kalund@ncsu.edu
[2] Theoretical Division, Los Alamos National Laboratory, Los Alamos, NM 87544, USA
[3] Joint Institute for Nuclear Astrophysics—Center for the Evolution of the Elements, USA
[4] Department of Physics and Astronomy, University of North Carolina, Chapel Hill, NC 27599, USA
[5] Center for Theoretical Astrophysics, Los Alamos National Laboratory, Los Alamos, NM 87544, USA
[6] University of Notre Dame, Notre Dame, IN 46556, USA
*Received 2022 August 18; revised 2022 December 16; accepted 2022 December 29; published 2023 February 21*

## Abstract

The rapid neutron capture process (*r*-process) is one of the main mechanisms whereby elements heavier than iron are synthesized, and is entirely responsible for the natural production of the actinides. Kilonova emissions are modeled as being largely powered by the radioactive decay of species synthesized via the *r*-process. Given that the *r*-process occurs far from nuclear stability, unmeasured beta-decay rates play an essential role in setting the timescale for the *r*-process. In an effort to better understand the sensitivity of kilonova modeling to different theoretical global beta-decay descriptions, we incorporate these into nucleosynthesis calculations. We compare the results of these calculations and highlight differences in kilonova nuclear energy generation and light-curve predictions, as well as final abundances and their implications for nuclear cosmochronometry. We investigate scenarios where differences in beta-decay rates are responsible for increased nuclear heating on timescales of days that propagates into a significantly increased average bolometric luminosity between 1 and 10 days post-merger. We identify key nuclei, both measured and unmeasured, whose decay rates directly impact nuclear heating generation on timescales responsible for light-curve evolution. We also find that uncertainties in beta-decay rates significantly impact age estimates from cosmochronometry.

*Unified Astronomy Thesaurus concepts:* R-process (1324); Nucleosynthesis (1131); Neutron stars (1108); Compact objects (288); Nuclear astrophysics (1129)

## 1. Introduction

Since its emergence in the 1950s, one of the biggest questions in the field of nuclear astrophysics remains the main production site of some of the heaviest elements, synthesized via the rapid neutron capture process (*r*-process; Burbidge et al. 1957; Cameron 1957). It is currently hypothesized that this process, thought to be responsible for roughly half the material heavier than iron, as well as the only process for producing the actinides, occurs to some extent in the neutron-rich outflows of neutron star mergers (NSMs). In addition to the many theoretical advances made in the last few decades, the recent electromagnetic observations accompanying the gravitational wave event GW170817 (Abbott et al. 2017a, 2017b; Díaz et al. 2017) lend the most support to the long-standing idea of a kilonova (KN) explosive transient powered by the radioactive decay of freshly synthesized *r*-process material (Lattimer & Schramm 1974, 1976; Li & Paczyński 1998; Metzger et al. 2010; Roberts et al. 2011; Barnes & Kasen 2013; Grossman et al. 2014; Wollaeger et al. 2018; Fontes et al. 2020).

The luminosity and morphology of the light curve associated with AT2017gfo (Chornock et al. 2017; Cowperthwaite et al. 2017; Nicholl et al. 2017; Perego et al. 2017) offer unique insight into the physics of these extreme environments. The bright but rapidly decaying component of the light curve observed at shorter wavelengths indicates at least some portion of ejecta material with little to no lanthanide or actinide abundances (Metzger et al. 2010; Roberts et al. 2011; Evans et al. 2017; Miller et al. 2019). On the other hand, a dimmer "red" signal that dominates on timescales of days (when the "blue" signal has faded away) indicates that at least some portion of the ejected material is composed of high-opacity lanthanides and possibly actinides (Barnes & Kasen 2013; Tanaka & Hotokezaka 2013; Kasen et al. 2017). These combined observations suggest distinct nucleosynthesis sites within the merger ejecta, each of which might be capable of producing a robust *r*-process pattern.

Despite the wealth of information provided by the data from GW170817, the larger endeavor of modeling KN signals for the purpose of reliably interpreting future signals remains subject to many unknown quantities and large uncertainties. While it is generally accepted that NSMs are a site for *r*-process production, it remains unclear whether these sites alone are capable of producing the entire observed *r*-process pattern. Studies of material ejected on dynamical timescales, via either tidal forces or compression between the coalescing neutron stars, predict material that is neutron-rich enough to produce out to the second and third *r*-process peaks (Rosswog et al. 1999; Goriely et al. 2011; Korobkin et al. 2012; Bauswein et al. 2013; Wanajo et al. 2014; Sekiguchi et al. 2015; Radice et al. 2018).

While there is general agreement on the robustness of *r*-process production in dynamically ejected channels, there is more uncertainty regarding the extent to which *r*-process production occurs in in late-time accretion disk outflows driven by viscous heating. Some part of this uncertainty comes from the central remnant scenario (Shibata et al. 2005; Agathos et al. 2020; Nedora et al. 2021; Kashyap et al. 2022). When prompt collapse does not occur, neutrino interactions are capable of

driving the $Y_e$ up enough to stifle *r*-process production. Neutrino oscillations can also play a large part in determining the extent of this effect, as only electron neutrinos act to reduce the neutron-richness of the ejecta (Malkus et al. 2012; Siegel & Metzger 2017; Li & Siegel 2021).

Simulating *r*-process nucleosynthesis is also subject to large uncertainties due to its trajectory far from nuclear stability where many important quantities remain unmeasured (Eichler et al. 2015; Martin et al. 2015; Mendoza-Temis et al. 2015; Mumpower et al. 2016b; Nikas et al. 2020). Detailed calculations incorporate nuclear heating contributions from multiple decay modes, and these impact the energy released, the thermalization efficiency with which the decay products deposit energy into the system, and the composition of material that is ultimately synthesized (Beun et al. 2008; Barnes et al. 2016; Mumpower et al. 2018; Even et al. 2019; Sprouse et al. 2020).

Of particular interest is the production of heavy nuclei that can undergo alpha decay or fission, especially when these are populated such that they decay on timescales whereby they compete with beta-decay heating. On timescales of days to weeks, nuclei of $A \sim 130$ contribute a large part of the beta-decay heating. However, the incorporation of theoretical spontaneous fission and alpha-decay rates has been found to largely impact the uncertainty in the nuclear heating on timescales relevant for the evolution of the red component of the light curve, in some cases adding up to an order of magnitude to the uncertainty (Goriely 2015; Vassh et al. 2019; Giuliani et al. 2020; Barnes et al. 2021; Zhu et al. 2021). These combine with additional uncertainties including the nuclear equation of state (Oechslin et al. 2007; Bauswein et al. 2013; Hotokezaka et al. 2013; Sekiguchi et al. 2015; Lehner et al. 2016), the nature of neutrino oscillations and neutrino transport in the ejecta (Ruffert et al. 1997; Foucart et al. 2016; Martin et al. 2018; Miller et al. 2019; Kullmann et al. 2021), as well as atomic line energy calculations for high-opacity lanthanides and actinides.

One particularly important data set for an *r*-process nucleosynthesis calculation is a description of the beta-decay rates involved (Möller et al. 2003; Caballero et al. 2014; Marketin et al. 2016; Shafer et al. 2016; Ney et al. 2020; Kullmann et al. 2022; Robin et al. 2022). At early times, the extent of *r*-process production is sensitive to the beta-decay rates of the nuclei involved, as these determine the relative abundances of connected isotopic chains during $(n, \gamma) - (\gamma, n)$ equilibrium and compete directly with neutron capture when equilibrium fails. At later times, and once a population of high mass number species is synthesized, beta-decay rates play a further role in determining the timescale of beta-decay chains, which are important for heating as well as for populating the species that contribute significantly to spontaneous fission and alpha-decay heating. Additionally, theoretical beta-decay rates can compete with theoretical alpha-decay and spontaneous fission branching ratios, which are crucial for determining the shape and magnitude of the light curve (Zhu et al. 2021).

In this work, we aim to incorporate different global beta-decay descriptions into nucleosynthesis calculations and compare their impact with those of other astrophysical and nuclear sources of uncertainty on nuclear energy generation, light-curve evolution, and predictions relevant to nuclear cosmochronometry. In Section 2, we describe the methods we use in generating and compiling nuclear data as well as the computational methods we use for calculating relevant quantities. We build upon the work and methods contained in Zhu et al. (2021), Barnes et al. (2021), whose work mainly focused on off-stability mass models and different fission prescriptions. For our astrophysical conditions, we aim to investigate the behavior of ejecta containing both high- and low-$Y_e$ material, expanding upon the models considered in, e.g., Kullmann et al. (2022), which focus on specific hydrodynamical simulations that tend to include more high-$Y_e$ material. In Section 3, we show the results of our calculations of nuclear energy generation and investigate cases of significant heating from heavy *r*-process alpha-decaying and fissioning nuclei on late-time light-curve evolution. We also show the broader impact these uncertainties in nuclear effective heating can have on a bolometric light curve. We conclude the presentation of our results with Section 4, in which we compute the age estimates for a selection of *r*-process-enhanced metal-poor stars using theoretically calculated abundances. Finally, we provide some concluding remarks in Section 5.

## 2. Method

We seek to quantify the leverage of beta-decay rates on key aspects of KN modeling when compared with other sources of nuclear and astrophysical uncertainty. The evolution of the nucleosynthetic abundances throughout the *r*-process determines the energy output in the form of nuclear heating. The thermalization profile of this released energy will determine how it is transported away from the system, which in turn affects the shape and magnitude of the observable light curve. The final abundance that is produced in a given merger event can then be used in a stellar dating technique if it is interpreted as being the sole source of a star's *r*-process material. In this section, we describe our data set and the methods used in the calculation of these quantities.

### 2.1. Model Set and Nucleosynthesis

We use the portable routines for integrated nucleosynthesis modeling (PRISM) to perform nucleosynthesis calculations using a suite of prepared input files describing astrophysical conditions and nuclear properties for a wide range of nuclei. The extent of *r*-process production is sensitive to the beta-decay rates of the nuclei involved, as these compete with neutron capture rates. Currently, many methods exist to compute beta-decay rates, but few are applied to large sections of the chart of the nuclides. In order to investigate the extent of the impact of different *global* sets of beta-decay rates in our calculations, we construct separate beta-decay and coupled beta-decay–beta-delayed fission reaction data sets consistent with three different beta-decay calculations, which we describe below.

The description contained in the work of Ney et al. (2020; calculations using these rates will hereafter be referred to as NES) uses the finite amplitude method with Skyrme density functionals to compute the beta-decay half-lives for neutron-rich species. These rates are an extension to Mustonen & Engel (2016), and include rates for all nuclei involved in the *r*-process as opposed to only even–even nuclei. This set of rates has not been used before in a parameterized study of *r*-process observables. The work of Marketin et al. (2016; hereafter MKT) uses a covariant density functional theory approach with Gogny interactions to do the same. Möller et al.

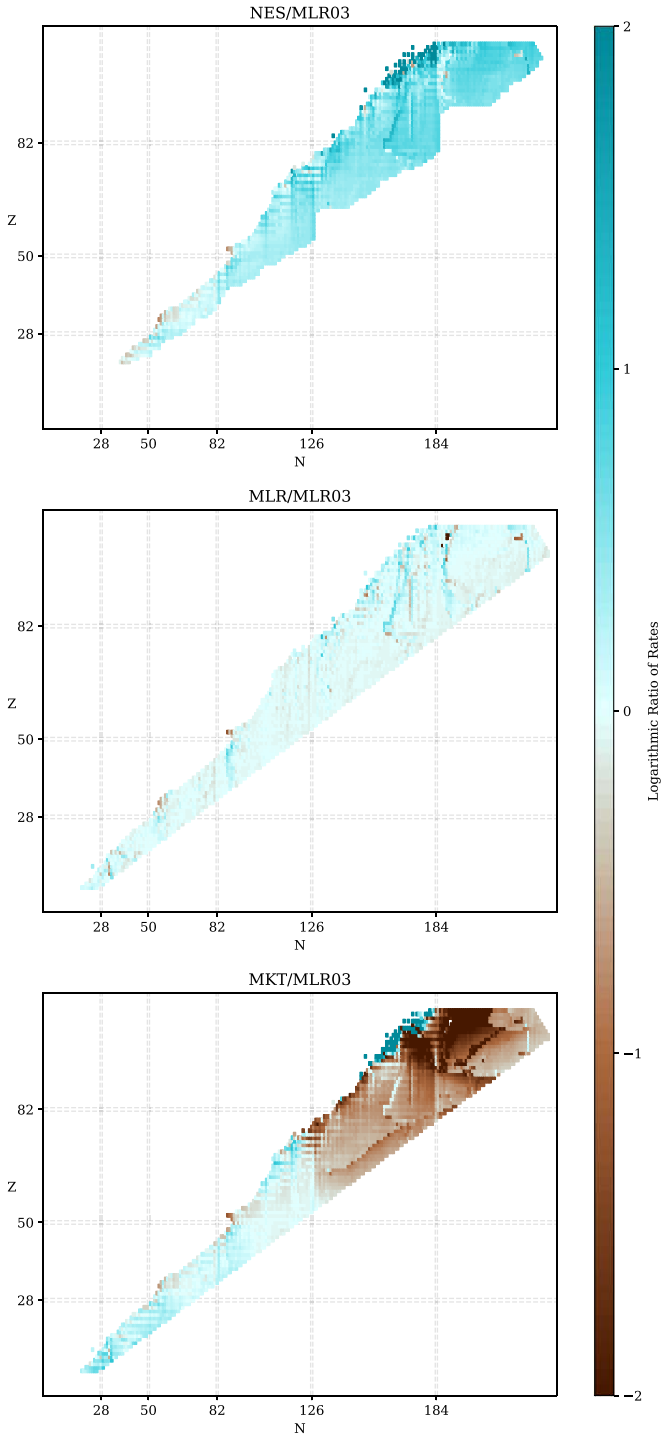


**Figure 1.** Logarithmic ratios of NES (top), MLR (center), and MKT (bottom) beta-decay rates with respect to MLR03 beta-decay rates. The color bar is adjusted to values of −2, 2 to reveal trends more clearly. The area covered by the Nubase 2016 data set (Audi et al. 2017) is removed.

(2019; hereafter MLR) uses a finite range droplet model in a quasiparticle random phase approximation to obtain $\beta$-strength functions for neutron-rich species. We use the three sets of beta-decay rates described and compute beta delayed neutron emission and beta-delayed fission probabilities and daughter product distributions using Mumpower et al. (2016a). We show the base-ten logarithm of the ratio of all three sets of beta-decay rates with respect to those of Möller et al. (2003; MLR03) in Figure 1. By using these three sets of rates, we are able to investigate the influence of a range of broadly fast (MKT) to broadly slow (NES) rates.

**Table 1**
Nuclear Mass Models (and Associated References) Used in Nucleosynthesis Calculations

| Abbreviation | References |
|---|---|
| DZ33 | Duflo & Zuker (1995) |
| ETFSI | Aboussir et al. (1995), Mamdouh et al. (2001) |
| FRDM2012 | Möller et al. (2016) |
| HFB22,HFB27 | Goriely et al. (2009, 2013) |
| SLY4 | Chabanat et al. (1998), Möller et al. (2015) |
| TF | Myers & Świątecki (1996, 1999) |
| UNEDF1 | Kortelainen et al. (2012), Möller et al. (2015) |
| WS3 | Liu et al. (2011), Möller et al. (2015) |

In addition to beta-decays, the nuclei involved in the *r*-process are also subject to other reactions and decays. The energy associated with these decays is important for the nuclear heating, and plays a large part in determining the shape and magnitude of the light curve. We calculate reaction and decay rates, as well as *Q*-values, consistent with the eight nuclear models listed in Table 1. We incorporate theoretical alpha-decay rates obtained using a Viola–Seaborg relation. We use neutron capture and neutron-induced fission rates calculated using the statistical Hauser-Feshbach code, CoH (Kawano et al. 2016).

For spontaneous fission rates, we use the barrier-height-dependent prescription from Karpov et al. (2012), Zagrebaev et al. (2011). We adopt mass models with appropriate fission barrier height descriptions: ETFSI (Aboussir et al. 1995) with ETFSI, Thomas–Fermi (TF; Myers & Świątecki 1999) with TF, HFB14 (Goriely et al. 2009) with HFB22 and HFB27, and FRLDM (Möller et al. 2015) for all others. We consider two possible fission fragment distributions; the first is a symmetric split, where the daughter products each equal one-half of the parent nucleus, while the second is the double Gaussian distribution described by Kodama & Takahashi (1975; hereafter K&T). We make an exception for the fission fragment distribution of the spontaneous fission of $^{254}$Cf, where we use the more detailed calculation from Zhu et al. (2018).

Finally, where experimental or evaluated data is available, we overwrite the theory rates with data from Nubase (Audi et al. 2017), and calculate *Q*-values using experimentally determined masses from AME2016 (Wang et al. 2017).

For the thermodynamic evolution of the ejecta, we use a parameterized wind model (Panov & Janka 2009) with an initial entropy per baryon of $s/k = 40$ and an expansion timescale of 20 ms. The network begins in nuclear statistical equilibrium with the initial seed nuclei determined using the SFHo equation of state (Steiner et al. 2013). In this work, we use the initial electron fraction, $Y_e$, as a proxy of variation in the astrophysical conditions of the ejecta in order to compare with uncertainties from the previously described variations from theoretical nuclear models. We note that a different choice of initial entropy per baryon or expansion timescale would likely have an effect on our results. While we acknowledge the importance of this question, it remains outside the scope of this work. We refer the reader to studies that explore this more carefully, including Just et al. (2015), Radice et al. (2018), Orford et al. (2022), and others.

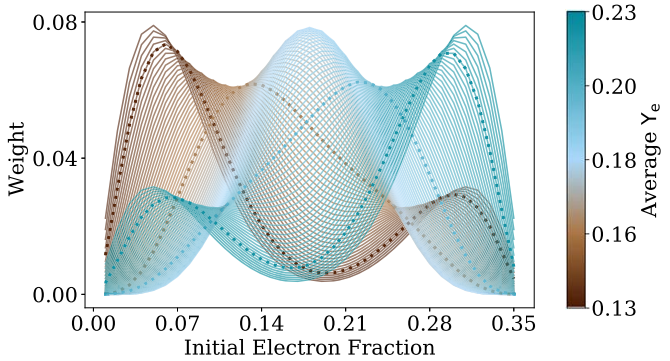


**Figure 2.** Distribution of combined single-$Y_e$ trajectories. The color of each line indicates the average $Y_e$ of the *combined trajectory*. A selection of combinations are shown as a guide to highlight the double-peak structures within the distribution. This color scheme is used throughout this work to refer to results for each combined trajectory, with the bluer combinations having less neutron-rich (low-$Y_e$) material and the more brown combinations having more neutron-rich material.

We use single-$Y_e$ trajectories with initial values of 0.02, 0.18, and 0.21 for the full suite of theoretical nuclear inputs. Based on the work in Zhu et al. (2021), we consider that these can be taken to represent varying degrees of contribution from fission to the total heating, with $Y_{e,i} = 0.21$ yielding the smallest contribution.

We also consider a set of trajectories to more closely model an ejecta with nonuniform composition. To do this, we perform nucleosynthesis calculations using the FRDM2012 and HFB22 subsets of nuclear inputs on single-$Y_e$ trajectories ranging from 0.01 to 0.35 in increments of 0.01. We map these onto an analytic probability distribution in order to sample a range of distributions with resulting average $Y_e$ values between 0.13 and 0.23. We show these mappings in Figure 2, and note that the resulting distributions contain both double-peaked distributions as well as single-peaked centered around a $Y_e$ of 0.18, as can be seen by the individual dashed lines in the figure. These distributions were obtained by combining two beta probability distribution functions and are described by the functional form

$$f(x, \alpha, \beta) = 2.5\left(\frac{\Gamma(\alpha+\beta)x^{\alpha-1}(1-x)^{\beta-1}}{\Gamma(\alpha)\Gamma(\beta)}\right) + \quad (1)$$

$$\left(\frac{\Gamma(\beta+\alpha)x^{\beta-1)}(1-x)^{\alpha-1}}{\Gamma(\beta)\Gamma(\alpha}\right), \quad (2)$$

where $\Gamma(\alpha)$ is the gamma function of $\alpha$. We vary the values of $\alpha$ and $\beta$ between 2.5 and 10.5.[7]

Previous work found that solar-like abundances can be obtained by combining individual trajectories with both high initial $Y_e$ as well as low initial $Y_e$ (Zhu et al. 2021). Our goal is not necessarily to obtain a solar-like final abundance pattern (we direct the reader to, for example, Ristic et al. 2022, which addresses *r*-process universality), since we do not know if KN events produce a solar pattern. Rather we aim to sample a variety of trajectories containing material with a variety of neutron richness, whether from dynamical ejecta plus disk outflows or from multicomponent disk outflows. This is consistent with most modern KN models predicting multiple ejecta components (see for example Just et al. 2015; Radice et al. 2016, 2018; Miller et al. 2019; Nedora et al. 2021; Stewart et al. 2022), while not constraining our investigation to any single hydrodynamical simulation.

We utilize these combinations of simulations for effective heating, as well as light-curve calculations out to 50 days. We also calculate late-time abundances (on the order of several Gyr), for cosmochronometry calculations (see Section 2.4).

### 2.2. Nuclear Heating

The evolution of the nuclear heating is given by coupling the energy from the radioactive decays with the efficiency with which their products thermalize. We therefore take the outputs from the nucleosynthesis calculations described and calculate the effective heating rate by combining the $Q$-value from the radioactive decays with the thermalization efficiency. We follow the method in Kasen & Barnes (2019), Zhu et al. (2021), with the total effective heating rate given by

$$\dot{Q}(t) = \sum_i \dot{q}_i(t) f_i(M_{\rm ej}, v_{\rm ej}, t) M_{\rm ej}, \quad (3)$$

where the sum is over all reactions and decays. The thermalization, $f_i$, is calculated as in Kasen & Barnes (2019) and is dependent on the ejecta mass and velocity. We use a total ejecta mass of 0.05 $M_\odot$ and an ejecta velocity of 0.15$c$.

### 2.3. Semianalytic Light-curve Model

We construct a semianalytic light-curve model following Zhu et al. (2021), Metzger (2020). We include some of the relevant details of the calculation here for convenience. We divide the ejecta into 100 layers with $0.1c < v < 0.4c$, with a velocity-dependent mass distribution and density profile given by

$$M_v = M_{\rm ej}\left(\frac{v_o}{v}\right)^3; \quad (4)$$

$$\rho(v, t) = \frac{3M_v}{4\pi v^3 t^3}. \quad (5)$$

The evolution of each shell is calculated independently using a forward-Euler scheme from 0.01 to 50 days post-merger, obeying

$$\frac{dE_v}{dt} = \frac{M_v}{M_{\rm ej}}\dot{Q}(t, v) - \frac{E_v}{t} - L_v. \quad (6)$$

The last term,

$$L_v = \frac{E_v}{t_{d,v} + t_{\rm lc}}, \quad (7)$$

is the luminosity of a shell and is dependent on the diffusion timescale, $t_{d,v}$, and the light-crossing time, $t_{\rm lc}$, of that shell:

$$t_{d,v} = \frac{M_{\rm ext}\kappa}{4\pi v t c}, \text{ and} \quad (8)$$

$$t_{\rm lc} = \frac{vt}{c}. \quad (9)$$

Here, $M_{\rm ext}$ is the mass exterior to the shell with velocity $v$. $\kappa$ is the opacity of the layer, which is calculated as a function of the temperature, $T_v$,

$$T_v = \left(\frac{E_v \rho(v, t)}{a M_{\rm norm}}\right)^{\frac{1}{4}} \quad (10)$$

[7] We use Scipy's (Virtanen et al. 2020) built-in beta function to generate these distributions.

**Table 2**
Names of Select r-ii Stars with Their Observed Abundances

| Star Name | $\log_\epsilon$(Eu) | $\log_\epsilon$(Th) | $\log_\epsilon$(U) | Reference(s) |
|---|---|---|---|---|
| HE1523-0901 | −0.62 | −1.2 | −2.06 | Frebel et al. (2007) |
| CS29497-004 | −0.66 | −1.16 | −2.20 | Hill et al. 2017 |
| CS31082-001 | −0.72 | −0.98 | −1.92 | Siqueira Mello et al. (2013) Hill et al. (2002) |
| J2038-0023 | −0.75 | −1.24 | −2.14 | Placco et al. (2017) |
| J0954+5246 | −1.19 | −1.31 | −2.13 | Holmbeck et al. (2018a) |

**Note.** These stars are sorted by increasing actinide enhancement.

of the layer, as follows:

$$\kappa = \begin{cases} \kappa_{\rm max}\left(\dfrac{T}{4000\ {\rm K}}\right)^{5.5}, & T < 4000\ {\rm K} \\ \kappa_{\rm max} & \text{otherwise.} \end{cases} \quad (11)$$

The value of $\kappa_{\rm max}$ depends on the composition of the ejecta. Specifically, the presence of lanthanides and actinides contributes large opacities, which are important for the *red* component of the light curve that is relevant on timescales of days (and the focus of this work). Given the temperature-dependent treatment that we have selected (as opposed to a "gray" opacity), we adopt a value of $\kappa_{\rm max}$ of 100 $\rm cm^2\ g^{-1}$ for all simulations, as this represents the scale of the maximum opacity from more detailed calculations of low-$Y_e$, lanthanide-bearing ejecta on timescales of a few days (Kasen et al. 2013; Tanaka et al. 2020).

### 2.4. Nuclear Cosmochronometry

The material produced in the NSM can act as a source of enrichment for a nearby stellar environment, i.e., the final abundance of an *r*-process-producing event can be taken as the initial abundance of a star. These can then be compared with spectral observations of stars, and a relation between the time of the enrichment event and the time of observation can be obtained by comparing the measured decay timescales and abundances of radioactive species (Butcher 1987). To this end, we compile a selection of five *r*-process-enhanced ([Eu/Fe] $> +1.0$), metal-poor ([Fe/H] $< -2$) stars of varying actinide richness, listed in Table 2.

From these observations, we use the measurements of europium ($Z = 63$), thorium ($Z = 90$), and uranium ($Z = 92$). We take the initial abundances to be those produced in an NSM and remaining 1 Gyr post-merger. Running the calculations out this long allows us to only rely on the theoretical abundances of the long-lived isotopes of thorium ($^{232}$Th) and uranium ($^{238}$U), which have half-lives of 14 and 4.47 Gyr, respectively. We compare these with the final abundances of the two most stable isotopes of europium ($^{151}$Eu and $^{153}$Eu).

If the NSM is taken to be the sole source of *r*-process enrichment, and is interpreted as occurring at $t = 0$, then the observed spectra can be interpreted as being taken at time $t$ given by the following relations:

$$t = 46.67\ {\rm Gyr}\ [\log_\epsilon({\rm Th/Eu})_0 - \log_\epsilon({\rm Th/Eu})_{\rm obs}]; \quad (12)$$

$$t = 14.84\ {\rm Gyr}\ [\log_\epsilon({\rm U/Eu})_0 - \log_\epsilon({\rm U/Eu})_{\rm obs}]; \quad (13)$$

$$t = 21.80\ {\rm Gyr}\ [\log_\epsilon({\rm U/Th})_0 - \log_\epsilon({\rm U/Th})_{\rm obs}]. \quad (14)$$

These relate the initial abundances, $\log_\epsilon({\rm X/Y})_0$, to observed abundances $\log_\epsilon({\rm X/Y})_{\rm obs}$. This approach, while useful, has a tendency to yield inconsistent results, especially when applied to actinide-boost stars, which are overabundant in thorium and uranium (Holmbeck et al. (2019) classifies these as having $\log_\epsilon({\rm Th/Dy}) > -0.90$).

We explore the impact of changing the description of beta-decay rates on the final abundance pattern where relevant for cosmochronometry calculations using the stars listed in Table 2 (all of which are notable for their detection of uranium). The abundance patterns we use to perform these calculations are constructed from the subset of individual trajectories using the FRDM2012 mass model, with initial electron fractions ranging from 0.01 to 0.35, as described in Section 2.1.

## 3. Effective Heating and Light Curve

We demonstrate the influence of beta-decay rates on the effective heating and the light curve by first considering the single-trajectory models that have a single value of the initial electron fraction. We then turn to the multitrajectory models that account for ejecta, which has a weighted range of initial neutron richness, as illustrated in Figure 2. In all cases, we take the total heating to be the summed contribution of the effective heating (as described in Section 2.2) from beta-decay, spontaneous fission, and alpha-decay reactions.

### 3.1. Single Trajectory

We begin with three different single-trajectory models, which are chosen to access different physics. The $Y_e = 0.02$ case is chosen to probe very neutron-rich ejecta that experiences fission cycling, where the daughter products of the first nuclei that fission capture enough neutrons to make it back to very heavy nuclei that will fission again. The $Y_e = 0.18$ case is chosen because a significant number of nuclei fission, but there is limited cycling, since at this $Y_e$ the number of neutrons is not enough to allow nuclei to fission twice. Finally, the $Y_e = 0.21$ case was chosen because material with this neutron richness makes a full *r*-process but does not have enough neutrons for much fission to occur.

The first row of Figure 3 shows the range of total heating curves resulting from these single-$Y_e$ trajectories of 0.02 (left), 0.18 (center), and 0.21 (right). The width of any one shaded band comes from the use of different mass models, and corresponding fission barriers, with each band color corresponding to one set of beta-decay rates from Figure 1. Overlap in the bands for different $Y_e$ cases appears as a darker region on the plot. An immediately noticeable trend is that the two lower-$Y_e$ cases have a wider spread in the prediction of total heating than the highest-$Y_e$ simulation does. In these lower-$Y_e$ cases, the NES simulations (darkest blue region) tend to show the highest *total* heating rates, i.e., they provide an upper limit for the total heating. Conversely, the MKT simulations (light blue region) tend to show less total heating and therefore provide a lower limit for the same.

To explore the reason for these effects, in the next three rows of the figure, we plot the contribution to the effective heating that stems directly from beta-decaying nuclei (second row), fissioning nuclei (third row), and alpha-decaying nuclei (bottom row). In all cases, the upper limit of the total heating shown in the top row is reproduced as a faint dashed line for comparison. The narrow width of the beta-decay heating bands,

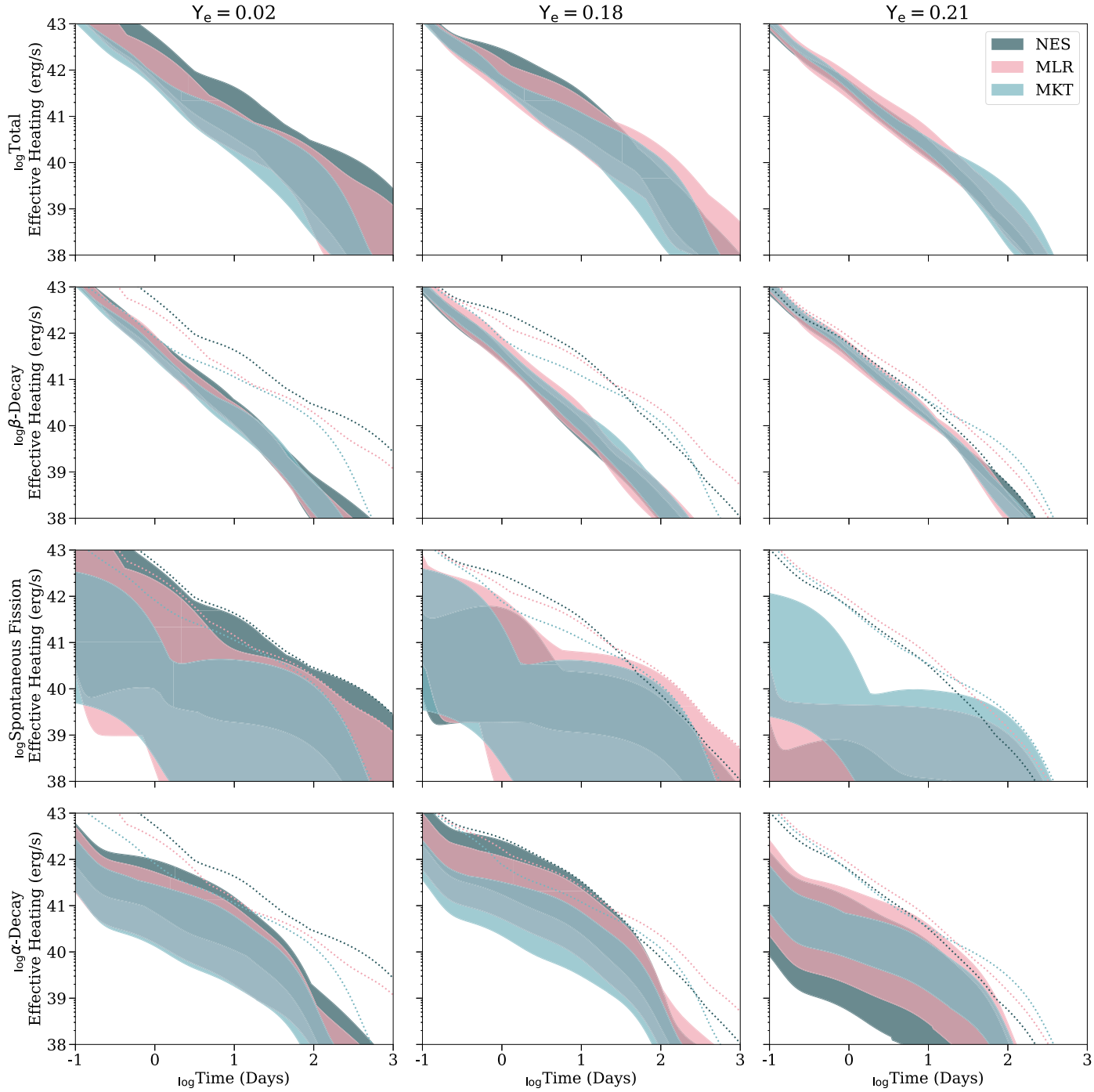


**Figure 3.** Range of effective heating rate predictions for all nuclear mass models from Table 1 when a single $Y_e$ trajectory is considered. Looking at the columns from left to right, the initial electron fraction increases from 0.02 to 0.18 to 0.21. The width of each band corresponds to the range of heating predictions for the NES (dark blue), MLR (pink), or MKT (light blue) simulations with the nine different mass models and both 50/50 as well as K&T fission daughter product distributions for which we calculate heating. For comparison, the maximum total heating is shown for each set of simulations as a series of dotted lines.

as well as their overlap, indicates that uncertainties in total effective heating, seen in the top row, cannot *directly* be attributed to differences in the beta-decay heating. The third and fourth rows of Figure 3 indicate that, in fact, the largest variation in total heating instead comes from differences in the contribution of spontaneous fission and alpha-decay heating. Looking at the right-most column, the $Y_e = 0.21$ case, we see that the total heating is dominated by beta decay, with alpha decay and spontaneous fission making up a relatively small portion of the total heating. As a consequence, the total heating for this case (top right) exhibits the least variation with different beta-decay rates. At about 1 day, this variation spans only about a factor of 2. However, looking at the left-most column ($Y_e = 0.02$), we see that fission can substantially affect both the total heating and the uncertainty in the total heating. The choice of beta-decay rates is *indirectly* but strongly influencing the total heating.

For some low-$Y_e$ simulations, the contribution of fission is subdominant, but for others, fission is the majority contribution, leading to the substantial spread in the results. Alpha

decay plays a similar role in the middle $Y_e$ cases (second column), where it largely controls the width of the band. The NES simulations contribute the upper limit in alpha decay in the middle $Y_e$ simulations as well as the upper limit to the heating at one day. Finally we note that the lower limits on the total heating, which are very similar between the three sets of beta-decay rates, occur in simulations with minimal alpha decay and fission, and are determined primarily by the beta-decay rates.

The shape and peak luminosity of the late-time ("red") light curve are expected to be substantially influenced by the evolution of the nuclear heating (Barnes et al. 2021; Zhu et al. 2021). Thus, as described in Section 2.3, we compute the evolution of the light curve on a timescale of days, out to 40 days post-merger. Analogous to Figure 3, we show the ranges of these results in Figure 4. We see that the beta-decay rates that produce the upper limit in the overall heating produce a corresponding upper limit in the light curve. Similarly, the range of uncertainty follows the pattern of heating bands with the largest variations coming from the lowest-$Y_e$ cases. It is interesting to note that, in the $Y_e = 0.21$ scenarios, the full range of variation is largely captured by the MLR rates.

While Figures 3 and 4 show the broad uncertainty in heating and light-curve evolution that can be obtained by changing the beta-decay rates, they do not show the specific simulations that are sensitive to these changes. The predictions of heating, and therefore of the light curve, for some mass models are relatively insensitive to the beta-decay rates. On the other hand, the predictions from other mass models show substantial sensitivity to the beta-decay rates. To illustrate this point, we have separated the total heating rate results by mass model in Table 3.

For easier comparison, we list the average ratio of total heating for NES:MLR and MKT:MLR. We also list the ratio of luminosity in parentheses, averaged over two different time periods: 1–10 and 10–100 days. For both the average heating as well as the average luminosity, we highlight those instances where using a different set of beta-decay rates results in a change of 50% or more in bold text. In the following discussion, we refer to these models with the format nuclearmodel.ye.

The heating at the later timescale of 10–100 days is in many instances dominated by the spontaneous fission of the long-lived $^{254}$Cf, which is a marker for actinide production. However, some models, such as the Hartree-Fock-Bogoliubov (HFB) models, facilitate the contribution from additional spontaneous fission heaters during this time. On the other hand, the models with lower fission barrier heights tend to suppress these extra possible contributions to the fission heating, leaving only that of $^{254}$Cf (Barnes et al. 2021; Zhu et al. 2021).

During the earlier time period of 1–10 days, the difference in total heating stems largely from competition between spontaneous fission, alpha-decay, and beta-decay heating. This highlights the sensitivity of some mass models to both $Y_e$ and beta-decay rates. For example, in the case of sly4.18, we find that the NES simulations show approximately 60% of the total heating coming from alpha decay by 5 days. Meanwhile, the corresponding MLR simulation is dominated by beta decay with a contribution from alpha decay that only rises to about

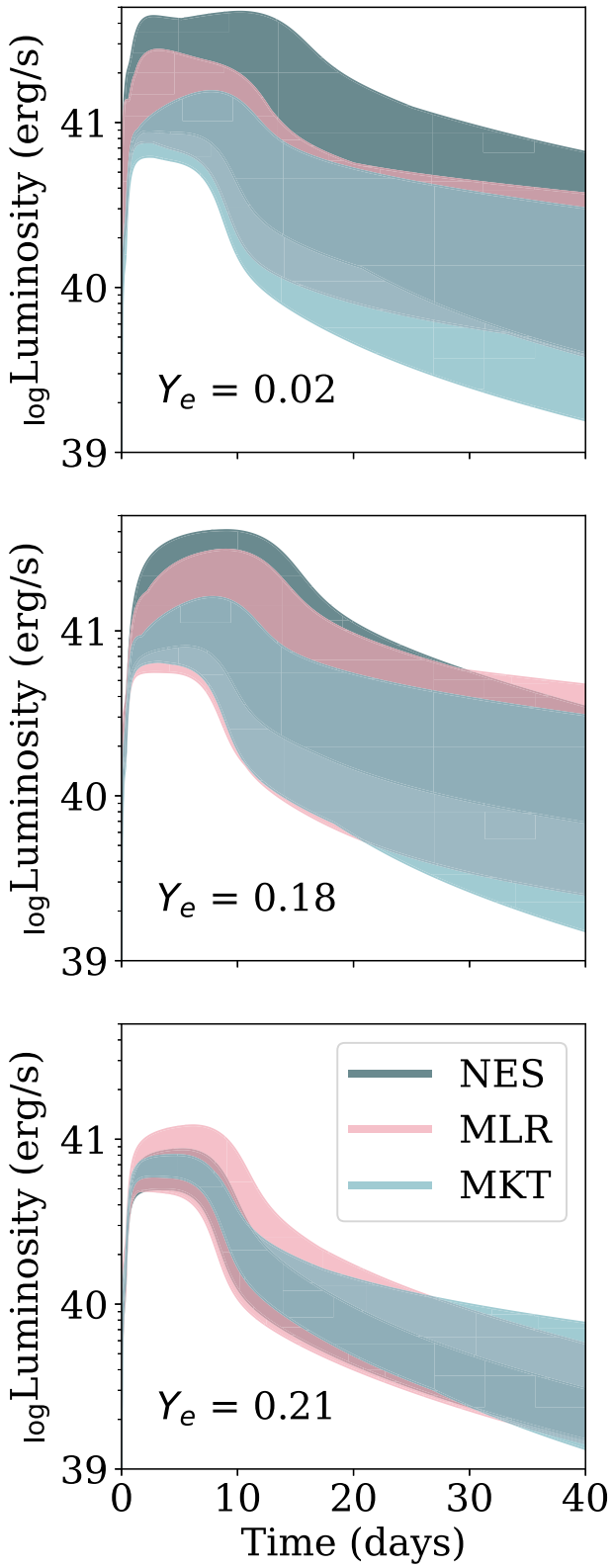


**Figure 4.** Uncertainty range of analytic light-curve models for all nine theoretical nuclear models from Table 1, when a single $Y_e$ trajectory is considered, with the calculation carried out to 40 days post-merger. The initial electron fraction increases from 0.02 to 0.18 to 0.21 from top to bottom. The width of each band corresponds to the range of luminosity predictions when the NES (dark blue), MLR (pink), or MKT (light blue) beta-decay rates are used, and include both 50/50 and KT fission yields.

40% by 7 days. Similarly, in the case of etfsi.18, the MLR simulations show more than 80% of the total heating coming from alpha decay as early as 2 days. When the MKT rates are used, there is still a significant contribution from alpha decay, but only up to a maximum of about 64% around 6 days.

In both these cases, it was the alpha decays of $^{212}$Po, $^{214}$Po, or $^{216}$Po that were among the top most significant contributors to the total heating. These lie in a region where nuclei undergo alpha decay on very short timescales and with a relatively large $Q$-value. Because of the very short timescales on which these decays occur, it is actually the populations of $^{224}$Ra and $^{222}$Rn (with half-lives of 3.6 and 3.8 days, respectively) that determine the overall contribution of the decays of their daughter polonium isotopes. The alpha-decay feeders into, for example, $^{224}$Ra and $^{222}$Rn decay on timescales that are too slow (with half-lives of 1.9 and 1600 yr, respectively) to be directly responsible for differences in heating on a timescale of a few days. Thus we conclude that the main source of differences lies in the unmeasured beta-decay rates feeding into $^{224}$Ra and $^{222}$Rn, as well as directly into $^{212–216}$Po (highlighted in Figure 5); these are critical for determining the amount of material that is available for alpha-decay heating, thereby determining the dominant source of total heating. We point out the consistency of this result with those of Wu et al. (2019).

We find that it is the cumulative effect of slight differences in the beta-decay rates in the large feeder region, rather than any one specific feeder nucleus. The use of overall slower rates (NES) feeding into this alpha-decay region resulted in a large enough heating contribution from alpha decay to dominate significantly over the beta-decay heating that determined the total heating (and light curve) at earlier times.

Spontaneous fission reactions occurring on timescales of days have the largest potential to make a significant difference in the overall heating, as well as the light curve, due to the large $Q$-values involved as well as the high thermalization efficiency of the reaction products. We find that, especially in the cases using the HFB theoretical nuclear models, spontaneous fission heating has the potential to dominate the total heating as early as 1 day post-merger. The enhanced heating seen in hfb22.02, hfb27.02, and hfb27.18, for example, can be attributed largely to differences in the predicted spontaneous fission heating rates. However, there is still a great deal of variety.

By 1 day post-merger, hfb22.02 shows approximately 77% of the total heating as coming from spontaneous fission heating, compared to only 33% at the same time in the corresponding MLR simulation. By 3 days, the spontaneous fission heating in the MLR simulation loses out to beta-decay heating, while the NES simulation shows it continuing to dominate the total heating out past 10 days. There are two mechanisms largely responsible for this behavior. One involves directly competing theoretical branching ratios for potential fission heaters. The colored regions of Figure 6 indicate where this occurs, and show the theoretical branching ratios for alpha decay, spontaneous fission, and beta decay. We found that the isotopes $^{272}$No and $^{271}$Lr appeared to consistently be responsible for a large part of the total heating in NES simulations. The significantly slower beta-decay rates predicted in these cases allowed for the spontaneous fission mechanism to compete with beta decay. Contrarily, the beta-decay rates predicted in MLR and MKT are fast enough to yield a beta-decay branching ratio of almost 100%.

**Table 3**
Average of the Ratios of Total Effective Heating Using NES or MKT to Total Effective Heating Using MLR Beta-decay Rates, over Different Time Periods

| | | 1–10 days | 10–100 days | | |
|---|---|---|---|---|---|
| Nuclear Model | $Y_e$ | NES | MKT | NES | MKT |
| SLY4 | 0.02 | **1.616** (1.338) | 0.856 (0.917) | **1.583** | 0.761 |
| | 0.18 | **1.797** (**1.642**) | 1.015 (1.217) | **2.662** | 0.937 |
| | 0.21 | 1.174 (1.112) | 1.469 (1.374) | 1.078 | 1.118 |
| UNEDF1 | 0.02 | 1.166 (1.231) | 0.823 (0.888) | 1.182 | 1.009 |
| | 0.18 | **1.517** (1.404) | 0.557 (0.657) | 1.027 | **0.454** |
| | 0.21 | 0.878 (0.904) | 1.167 (1.16) | 0.801 | 1.125 |
| DZ33 | 0.02 | **1.674** (1.459) | 0.678 (0.82) | **2.224** | 1.089 |
| | 0.18 | **1.631** (1.416) | **0.432** (0.549) | 0.938 | 0.849 |
| | 0.21 | **0.416** (0.504) | 0.656 (0.709) | **0.384** | 1.376 |
| ETFSI | 0.02 | 1.114 (1.042) | 0.553 (0.683) | **1.779** | 1.432 |
| | 0.18 | 1.24 (1.179) | **0.333** (**0.499**) | **1.799** | 0.841 |
| | 0.21 | 0.923 (0.914) | 1.241 (1.263) | 1.12 | 1.249 |
| FRDM2012 | 0.02 | 1.27 (1.089) | 0.548 (0.752) | 1.438 | 0.633 |
| | 0.18 | 1.377 (1.261) | **0.453** (0.556) | 0.785 | **0.333** |
| | 0.21 | 0.538 (0.589) | 0.642 (0.692) | **0.318** | 0.822 |
| HFB22 | 0.02 | **6.591** (**2.806**) | 1.215 (0.529) | **4.528** | **1.501** |
| | 0.18 | 1.069 (0.993) | **0.412** (0.551) | **0.437** | **0.333** |
| | 0.21 | 0.895 (0.902) | 1.177 (1.2) | 0.949 | **3.147** |
| HFB27 | 0.02 | **2.002** (**1.74**) | **0.26** (**0.348**) | **2.085** | **0.399** |
| | 0.18 | 1.177 (1.083) | **0.302** (**0.462**) | 0.697 | **0.299** |
| | 0.21 | 0.962 (0.952) | 1.264 (1.27) | 1.011 | **3.158** |
| TF | 0.02 | 1.25 (1.068) | **0.406** (**0.761**) | 1.171 | **0.406** |
| | 0.18 | 1.078 (1.11) | 0.586 (0.786) | **1.818** | **0.364** |
| | 0.21 | 0.642 (0.719) | 0.54 (0.634) | 0.584 | **0.282** |
| WS3 | 0.02 | **1.549** (1.277) | 0.729 (0.856) | **1.918** | 0.976 |
| | 0.18 | 1.293 (1.253) | 0.578 (0.664) | 0.709 | 0.828 |
| | 0.21 | 0.886 (0.893) | 1.389 (1.33) | 1.131 | **4.588** |

**Note.** In the 1–10 days column, the average ratio of bolometric luminosity is listed in parentheses. Bold-faced values indicate an average change of ±50% or more.

The isotopes of rutherfordium ($Z = 104$) appeared to contribute to different degrees in the NES and MLR calculations, yet were not among the top heaters in the MKT calculation. In NES calculations, the heavier isotopes ($N = 168$, 169, 172) appeared to contribute the most to the total heating at early times. For example, the spontaneous fission of $^{273}$Rf alone was responsible for approximately 28% of the total heating at 1 day post-merger. On the other hand, it was the "lighter" isotopes ($N = 166$, 167) that contributed the most to the total heating in MLR calculations, and did so for a more extended period of time in both MLR and NES calculations.

We attribute this to the second mechanism responsible for differences in the role of fission in our calculations: differences in feeder decay chains that build up different abundances available for decay. One very obvious example of this is that of $^{271}$Db. This isotope only appears in the MLR calculation, as this is the only one in which decay into it is allowed. Furthermore, in the MLR calculation in which it appears, the heating from its decay via spontaneous fission competes with or even exceeds that of the alpha decay, despite a very small fission branching.

This difference in populations also affects the extent to which fission heaters with measured rates are able to contribute

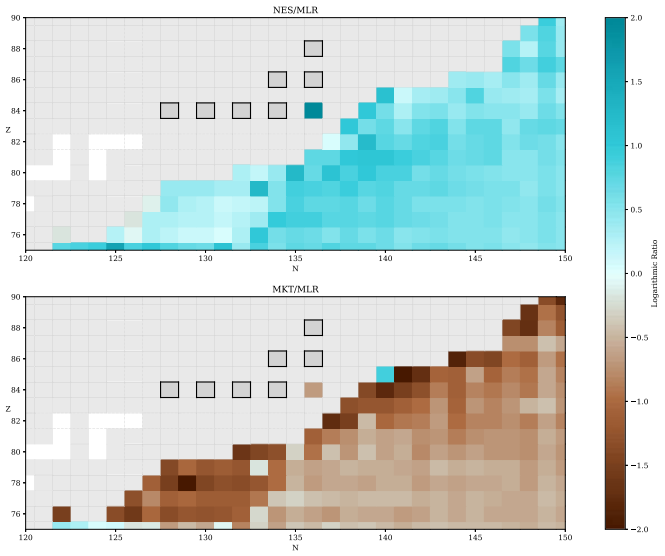


**Figure 5.** Ratio of beta-decay rates used in NES:MLR (top); or MKT:MLR (bottom) calculations in the region feeding into important alpha-decay heaters (outlined in black boxes) identified in, for example, sly4.18. We show here only the rates subject to theoretical models; those covered by the Nubase2016 data set are shown in gray.

to the total heating. These are also highlighted in Figure 6, and include $^{254}$Cf, $^{256}$Cf, and $^{259}$Fm.

In the MKT calculation, the population of $^{259}$Fm is blocked via beta decay. The population of its alpha-decay feeder, $^{263}$No, is also blocked via beta decay, resulting in $^{259}$Fm not being able to contribute significantly to the heating in MKT calculations. However, in NES calculations, enough material is able to decay into $^{259}$Fm such that its contribution to the spontaneous fission heating is significant; alone it is responsible for roughly 38% of the total heating at 2 days post-merger.

While these calculations represent the results obtained by using a single-$Y_e$ trajectory, they highlight the influence that the choice of mass model can have when combined with $Y_e$. The use of certain mass models with a given $Y_e$ unlocked a wide variety of potential heaters that impacted the evolution of the light curve. We emphasize that experimental data for several of these unmeasured isotopes would prove highly valuable in constraining this uncertainty.

### 3.2. Combined Trajectories

Since it is expected that element synthesis will occur in outflows with a range of electron fractions, we now turn to the variation in outcomes that is produced by employing different sets of beta-decay rates in scenarios with multiple trajectories but using a single mass model. Accordingly, Figure 7 shows the abundances for nuclei $Z > 50$ obtained at 10 Gyr post-merger from the linear combinations of individual $Y_e$ trajectories (*combined trajectories*) using *only* the FRDM2012 mass model, as described in Section 2.1. The coloring of the individual lines corresponds to those in Figure 2, i.e., more brown representing a combination weighted toward low-$Y_e$ and bluer representing one weighted toward high $Y_e$. The left, center, and right columns represent NES, MLR, and MKT simulations, respectively. The top and bottom rows show results using 50/50 and K&T fission yields, respectively. We note that in all cases we have a substantial fraction of high-$Y_e$ ($Y_e > 0.2$) material that has little to no fission.

As in the previous section, we are interested in investigating the evolution of the nuclear heating for these combined trajectories and its impact on the light curve. The large panels of Figure 8 show the heating as a function of time for each of the combined trajectories. Similar to the ratios shown in Table 3, we compute the ratio of the heating for each combined trajectory when NES and MKT beta-decay rates are used compared to MLR. We show these graphically in Figure 8. Because of the potentially large contribution from fission to the heating, we also perform a set of similar calculations using *only* the HFB22 mass model. Figure 9 shows the evolution of the heating when this mass model is used.

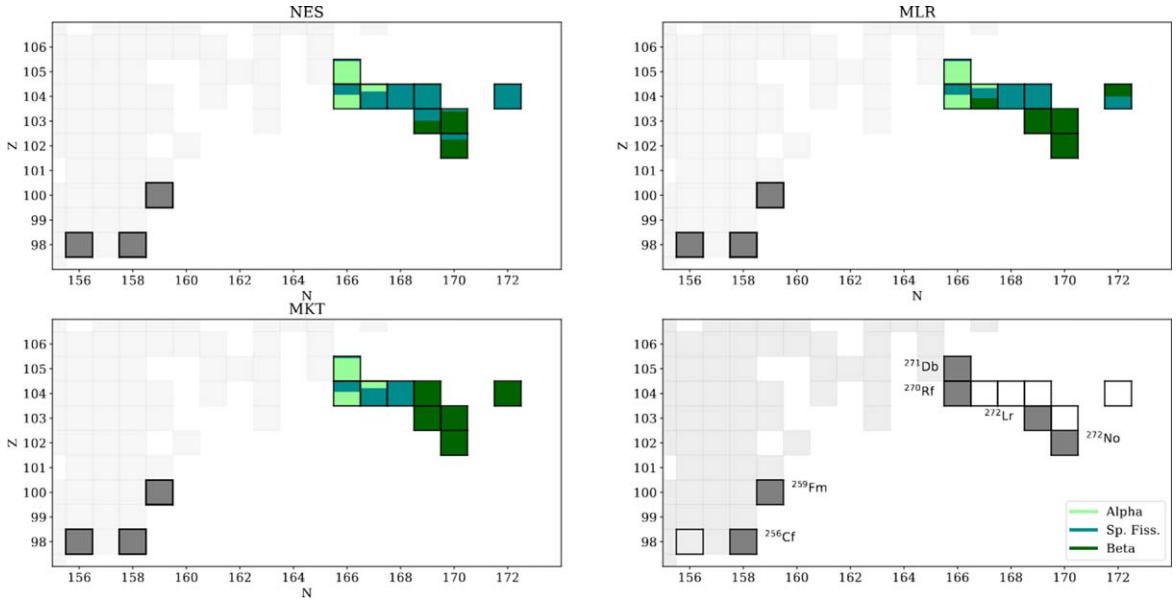


**Figure 6.** Theoretical branching ratios for a selection of key nuclei that have the potential to be important spontaneous fission heaters, as identified in, for example, hfb22.02. The gray-filled isotopes have experimentally determined values; the colored isotopes remain unmeasured. Light green, teal, and dark green represent the branchings expected for alpha decay, spontaneous fission, and beta decay, respectively. In the bottom right panel, we show the chemical names for highlighted isotopes for ease of identification.

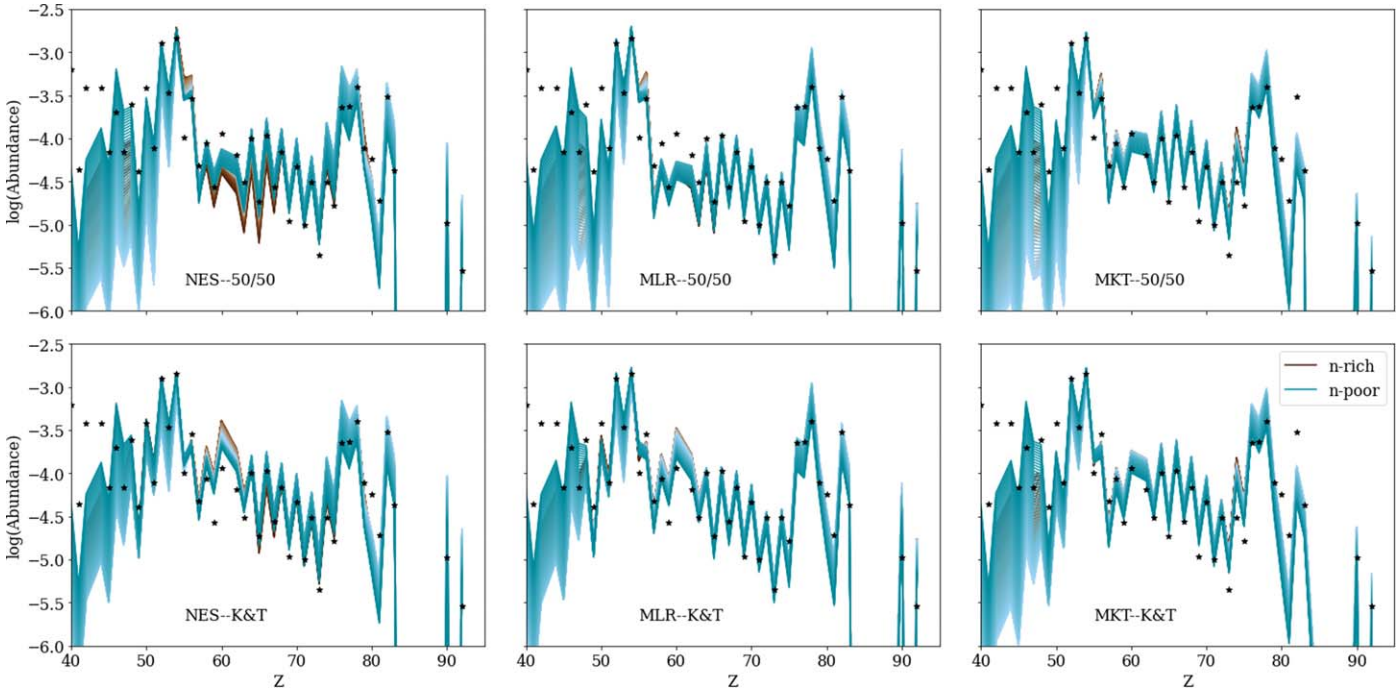


**Figure 7.** Abundance patterns at 10 Gyr for combined trajectories displayed in Figure 2 using the FRDM2012 mass model, with the same coloring convention (brown representing more neutron-rich combinations, and blue more neutron-poor). Solar *r*-process residuals (Asplund et al. 2009) are plotted as black stars, scaled such that the abundance of bromine ($Z = 35$) is $10^{-2.5}$.

As in Figure 3, the top row of Figures 8 and 9 shows the total heating for each of the combined trajectories, with the ratio to MLR immediately underneath for NES and MKT calculations. Similarly, the second, third, and fourth rows show the individual contributions from beta-decay, spontaneous fission, and alpha-decay heating, respectively. As before, the total heating is shown as faint gray lines for comparison.

When the FRDM2012 mass model is used, we find the heating out to at least 1 day is dominated by beta decay for all three beta sets of beta-decay rates. As expected, this varies more when the HFB22 model is used, and we find more of a dependence on the beta-decay model used. Furthermore, in the FRDM2012 case, the beta-decay heating is roughly independent of the combined trajectory, as can be seen from the relatively narrow width of the bands in the second row of Figure 8. The ratios of the beta-decay heating with NES or MKT, compared to MLR, tend to stay close to 1.

Each of the composite trajectories has a significant amount of high-$Y_e$ material, and this can *dilute* the heating contributions from spontaneous fission and alpha decay. Indeed, when the FRDM2012 model is used, the spontaneous fission heating does not appear to significantly dominate the shape of the total heating until tens of days, for any of the combined trajectories. We find the most potential for early time (order days) contribution to the total heating from spontaneous fission in the low-$Y_e$ weighted NES simulations. This is reflected in the cases where the HFB22 model is used; the lowest average $Y_e$ NES calculations show the most robustly dominant contribution from spontaneous fission. Similarly, the effect of the alpha-decay heating is diluted enough that for no combined trajectory does it ever dominate the total heating, whether the FRDM2012 or HFB22 model is used. However it is apparent from Figures 8 and 9 that the description of the total heating is not complete without accounting for both the spontaneous fission as well as the alpha-decay heating.

We see the combined trajectories with the largest proportions of the lowest-$Y_e$ material showing the most spontaneous fission heating. As a larger proportion of high-$Y_e$ material is included, we begin to see this dilution effect, and the amount of spontaneous fission heating decreases accordingly. Section 3.1 also showed the largest amount of alpha-decay heating in the *semi-neutron rich* ($Y_e$ of 0.18) case. This behavior is reflected in the fourth rows of Figures 8 and 9, and is most apparent for the NES simulations. There is an increase in the contribution of alpha-decay heating as more neutron-rich material is included until a point where the material becomes too neutron-rich, and the material is more efficiently deposited into the higher-$Z$ fissioning region, thus contributing less to the alpha-decay heating.

In the case of both spontaneous fission and alpha decay, the point in time at which all these effects occur depends on the beta-decay rates. For example, the number of days after the merger at which beta decay no longer closely approximates the total heating occurs sooner in NES simulations than that in MLR, which in turn occurs sooner than that in MKT simulations. We find that the contribution of alpha-decay heating has the most potential to be significant in NES simulations that are more heavily weighted toward the middle of our $Y_e$ range. There is also a more significant difference between the potential for significant alpha-decay heating for mid-$Y_e$ combined trajectories compared to those weighted toward low $Y_e$ for NES simulations than both MLR and MKT simulations. In these latter cases, there is more similarity between low- and mid-$Y_e$ weighted combined trajectories. This is consistent with the result obtained in Section 3.1, where we found the largest contribution to alpha-decay heating to be in the $Y_e = 0.18$ case in NES simulations.

We find that the use of a different set of beta-decay rates changes the timescales on which these differences appear, and the extent to which they affect the total heating. However,

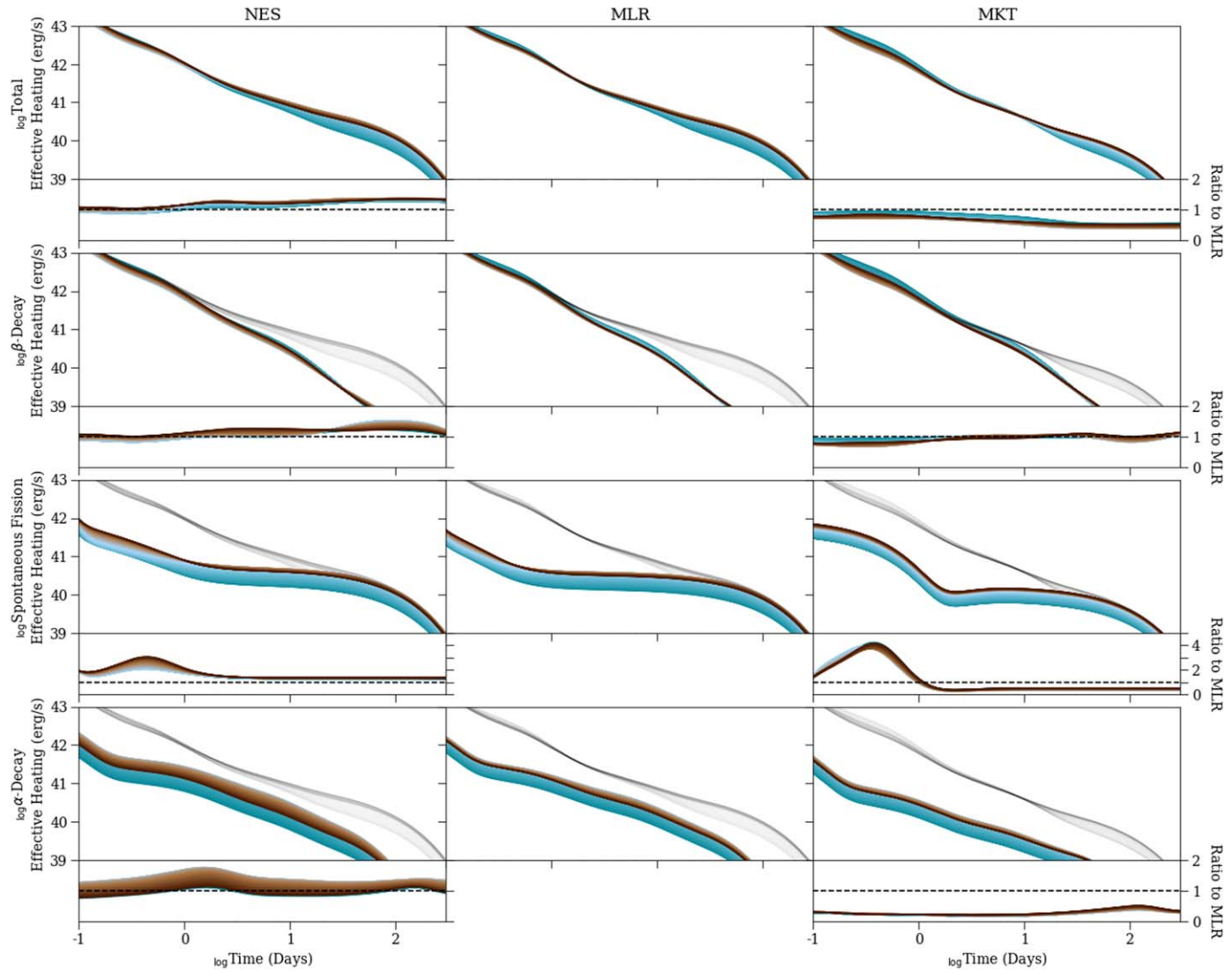


**Figure 8.** Range of effective heating rate predictions using the FRDM2012 mass model with 50/50 fission product yields when composite-$Y_e$ trajectories are considered. From left to right, the beta-decay description used is NES, MLR, MKT. The color scheme corresponds to that shown in Figure 2. As in Figure 3, we replicate the total heating curves shown in the top row in the bottom three rows as light gray lines for easier comparison.

when these differences are propagated through the light-curve calculations, we find that the differences are more subtle. We show the light curves resulting from the combined trajectory effective heating results in Figures 10 (for the FRDM2012 case) and 11 (for the HFB22 case), following the same coloring convention as the heating. The left, middle, and right panels show the light curves for NES, MLR, and MKT simulations, respectively. In all three cases, we find that the overall shapes of the light curves are consistent for all three sets of beta-decay rates, e.g., there are no plateaus or bumps present in some but not others.

When comparing beta-decay rates, for a given mass model, the most apparent difference in the light curves lies in the behavior after approximately 4 days. The NES and MLR simulations show similar behavior with the NES simulations yielding a higher peak luminosity for mid- to high-$Y_e$ weighted combined trajectories. In addition to a smaller peak magnitude, the low-$Y_e$ weighted combinations show an earlier peak than the more neutron-rich trajectories. Furthermore, these tend to decay more quickly. The MKT calculations yield slightly different results, with the lowest-$Y_e$ material yielding the largest peak magnitude. This is consistent with the total heating behavior observed in the MKT simulations, shown in the top row of Figure 8. We attribute this to the dominant heating mechanisms in MKT calculations being beta decay for a longer period of time, which is largest in the higher-$Y_e$ weighted trajectories. Thus the alpha-decay heating contribution, which is largest for low-$Y_e$ dominated trajectories, is unable to compete until later in time. This point is reflected in the MKT light curves, in which there is a flip, and the low-$Y_e$ trajectories have the highest luminosity. This is also apparent when comparing between mass models. The combined effect of the NES beta-decay rates and the HFB22 model facilitating a large contribution from fission heating yields a significantly larger peak magnitude in the light curve than that of the same beta-decay rates and the FRDM2012 model. Contrarily, even with the HFB22 model, the use of the MKT beta-decay rates yields a comparatively small contribution from fission, and the light-curve predictions do not vary much between mass models.

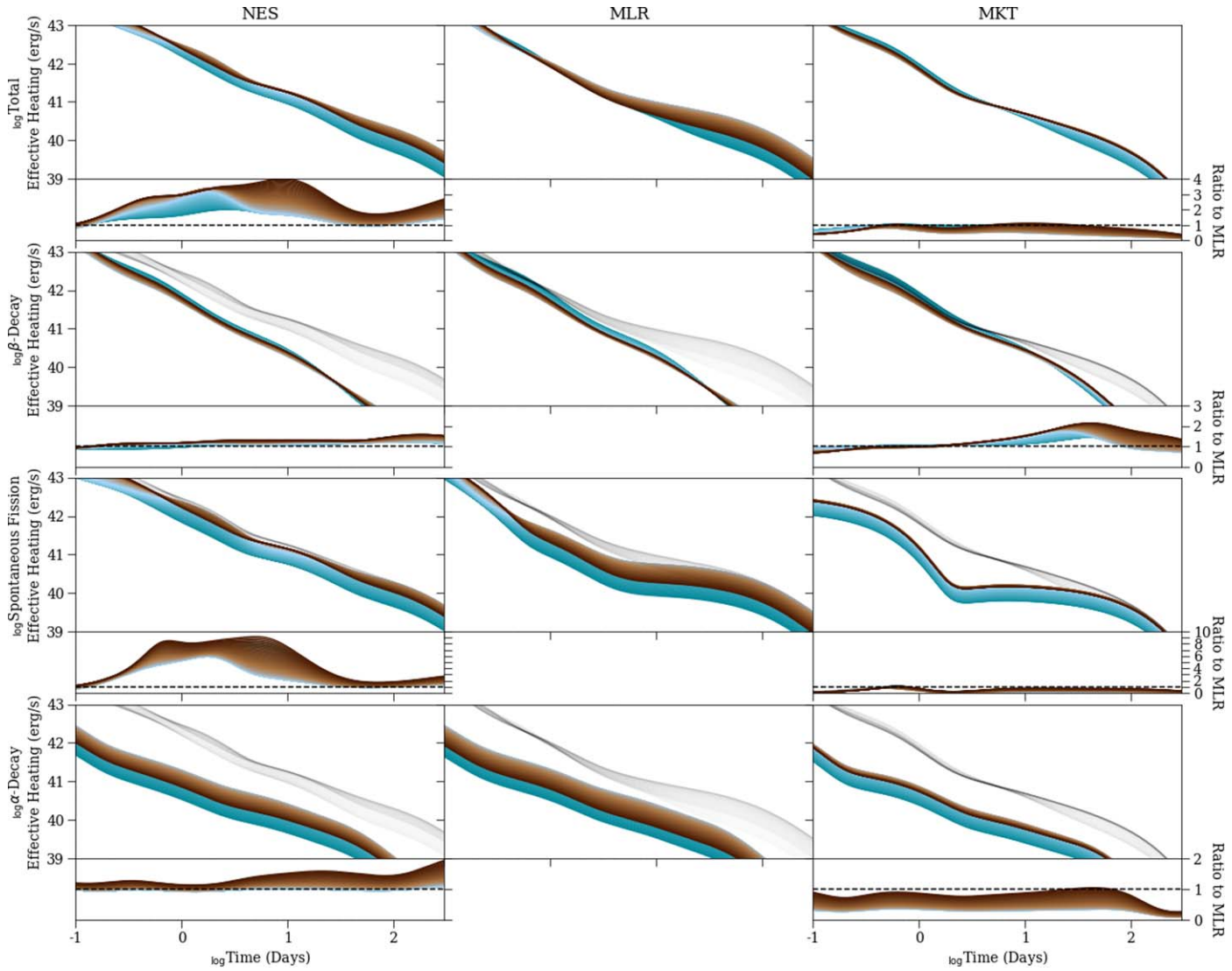


**Figure 9.** Range of effective heating rate predictions using the HFB22 mass model when composite-$Y_e$ trajectories are considered with 50/50 fission product yields. From left to right, the beta-decay description used is NES, MLR, MKT. The color scheme corresponds to that shown in Figure 2. As in Figure 3, we replicate the total heating curves shown in the top row in the bottom three rows as light gray lines for easier comparison.

## 4. Applications for Nuclear Cosmochronometry

Using the same combined trajectories described in Section 2.1, and using only the FRDM2012 mass model, we calculate the ages[8] of a selection of *r*-process-enhanced, metal-poor stars, as described in Section 2.4. We show the range of results of these calculations in Figure 12. We emphasize that the choice of mass model will quantitatively influence the results shown in Figure 12, and the analysis here is presented only for FRDM masses. The left and right columns of Figure 12 use the 50/50 and K&T fission yields, respectively. Each row shows the results for a different star, with actinide-richness increasing from HE1523 (most actinide-deficient) to J0954 (most actinide-boosted). To obtain these ranges, we use the quoted observational values in Table 2 for $\log_\epsilon(\mathrm{X/Y})_{\mathrm{obs}}$ and the theoretical abundances obtained at 1 Gyr post-merger from each individual combined trajectory for $\log_\epsilon(\mathrm{X/Y})_0$. For the purposes of Figure 12, we have not included observational uncertainties. We do so later in this section.

Theoretical beta-decay rate predictions are a critical component of parameterized cosmochronomotery studies (Goriely & Arnould 2001; Schatz et al. 2002; Holmbeck et al. 2018b, 2019; Eichler et al. 2019). For example, the use of theoretically calculated lanthanide *and* actinide abundances can yield age estimates that show a substantial spread depending on the choice of beta-decay rates (Holmbeck et al. 2018b). We show this effect using our calculations in Figure 12. In this figure, we show the maximum uncertainty in age for the five stars in Table 3 from NES (dark blue), MLR (pink), and MKT (light blue) calculations using all three chronometer pairs.

Use of the rare-Earth—actinide chronometer pairs with NES or MLR simulations tends to produce age estimates that are high relative to the actinide-only chronometer. This effect is most pronounced in actinide deficient stars, as can be seen from top row of Figure 12.

We attribute this to an overproduction of actinides relative to rare Earths, as shown in Figure 13, where we have plotted the composite, i.e., for the combined trajectories, abundances of

[8] We use *age* as a concise way to refer to the time since the enrichment event, not *necessarily* the time since the formation of the star itself.

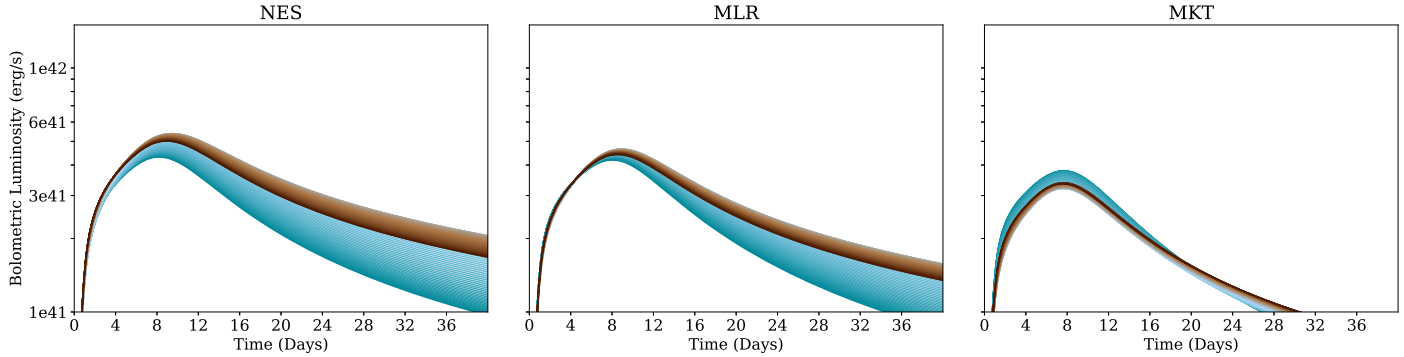


**Figure 10.** Uncertainty range of analytic light-curve models for FRDM2012 nuclear model with multiple-$Y_e$ composition using 50/50 fission product yields. From left to right, the beta-decay description used is NES, MLR, MKT. The color scheme corresponds to that shown in Figure 2, with the most striking blue representing the behavior of the most neutron-poor material, and the darkest brown that of the most neutron-rich material.

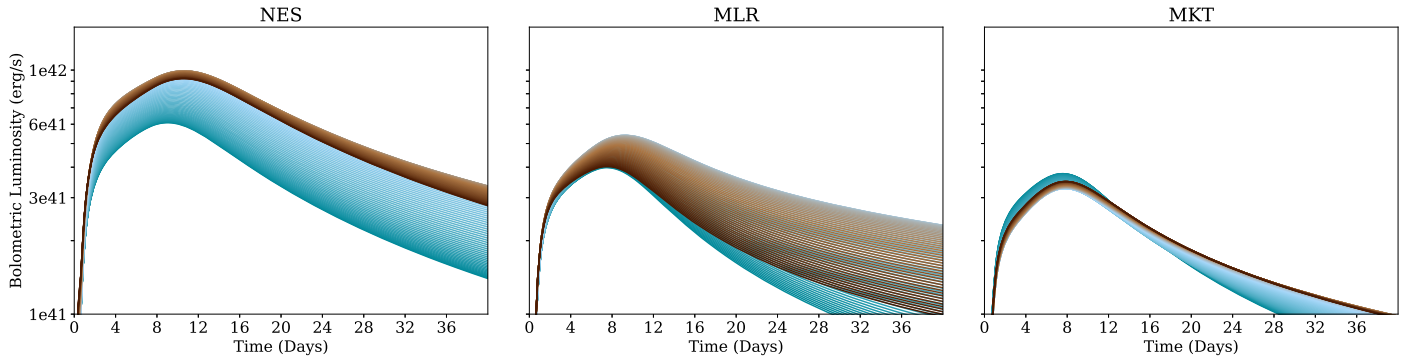


**Figure 11.** Uncertainty range of analytic light-curve models for HFB22 nuclear model with multiple-$Y_e$ composition using 50/50 fission product yields. From left to right, the beta-decay description used is NES, MLR, MKT. The color scheme corresponds to that shown in Figure 2, with the most striking blue representing the behavior of the most neutron-poor material, and the darkest brown that of the most neutron-rich material.

europium (red), thorium (teal), and uranium (pink). The overproduction is largest for the 50/50 fission yields. This effect is ameliorated with the use of the K&T fission yields because this model spreads out the fission daughter nuclei over a larger range of mass number. In all cases, for a more actinide deficient star, the amount of time that is necessary for the overproduced actinide content to decay to match the observed abundances is larger. We see this reflected in Figure 12, where the stars are sorted in order of increasing ratio of actinide to rare-Earth abundance.

In contrast, the use of MKT beta-decay rates in some astrophysical conditions yields theoretical initial production (Th/Eu) values that are lower than those observed in some stars. This results in lower ages when Equations (12) and/or (13) are applied, as compared with the actinide-only chronometer pair. As can be seen in Figure 13, MKT tends to produce simultaneously less actinides and more rare Earths than do other theoretical formulations of beta-decay rates. This effect is most pronounced for stars with a larger actinide enrichment, such as CS31082 and J0954. Again, the effect is mitigated slightly when using the more diverse fission daughter product distribution (K&T), which increases somewhat the predicted europium yield, as well as the yields between $57 < Z < 63$. Indeed, the europium production in K&T simulations shows less sensitivity to beta-decay rates than the simulations with the 50/50 fission daughter product distribution. The lower actinide population in MKT calculations is consistent with those of previous works (Holmbeck et al. 2018b; Eichler et al. 2019; Barnes et al. 2021; Zhu et al. 2021), where the relatively fast MKT beta-decay rates above the $N = 126$ shell closure (which can be seen in Figure 1) were found to inhibit the buildup of a significant actinide population.

### 4.1. Actinide Constraint

While the use of actinide–lanthanide ratios yield a large spread of results, thorium and uranium are generally produced concomitantly (as can be seen, for example, in their abundance behavior in Figure 13), resulting in smaller uncertainties. This feature, and the resulting usefulness of the U/Th chronometric pair has long been discussed in the literature; see, for example, Goriely & Arnould (2001), Ren et al. (2012), and Holmbeck et al. (2018b).

In Figure 14, we focus on this uncertainty; these results were obtained solely from using variation in the theoretical values of $\log_\epsilon$(U/Th) in our models. Each colored bar corresponds to the range of results we obtain using NES (dark blue), MLR (pink), and MKT (light blue) simulations, along with the 50/50 (plotted on the left) and K&T (plotted on the right) fission yields. We find from this figure that there is more star-to-star variation, than variation from the use of different beta-decay rates, fission descriptions, or combined trajectory sets.

We also find here that similar actinide abundances are produced in NES and MLR simulations, while MKT shows consistently different behavior. The NES and MLR simulations produced comparable amounts of thorium as well as uranium, with NES simulations never exceeding a factor 0.8–1.3 times the corresponding MLR simulation abundance. The result of

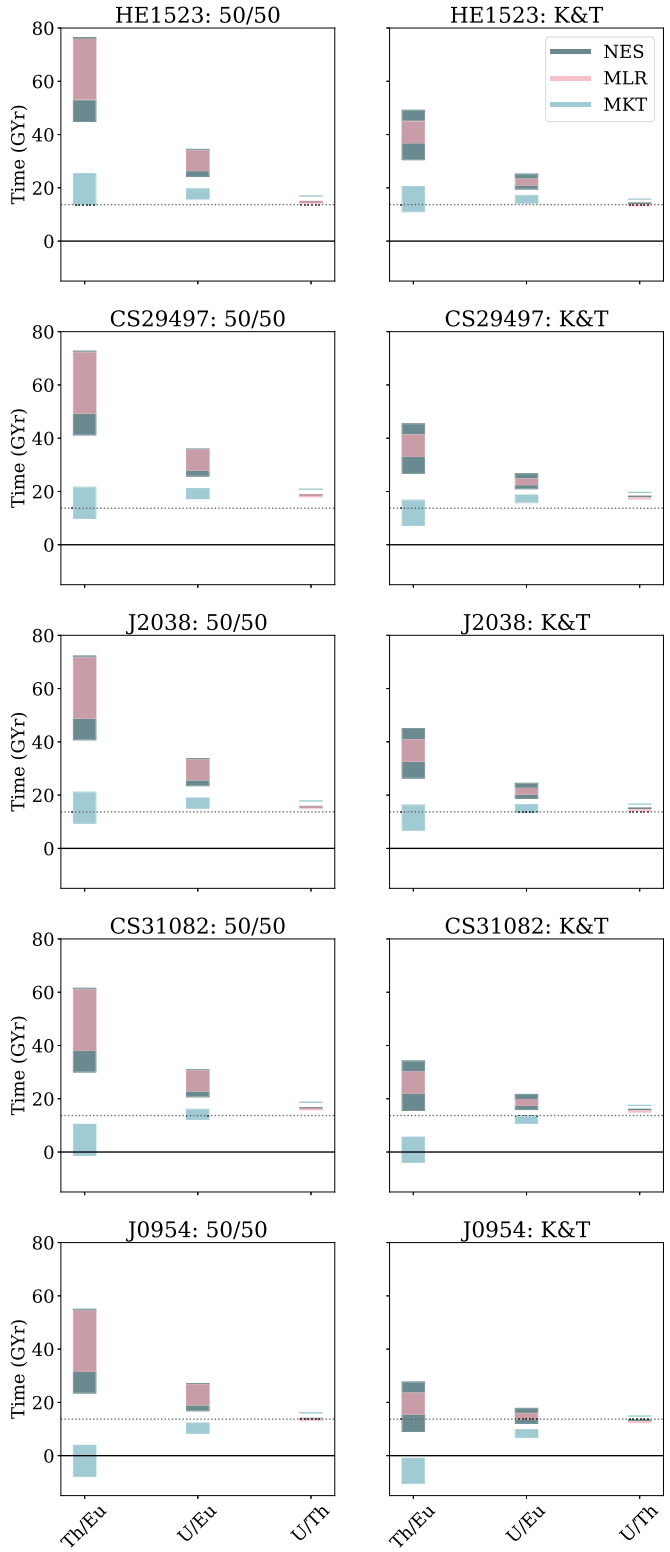


**Figure 12.** Maximum uncertainty from the use of different beta-decay rates for the stars listed in Table 2, with each row corresponding to a different star. The left column shows ages computed using the 50/50 fission yields, while the right column contains those obtained using the K&T fission yields. As throughout this work, NES calculations are shown in dark blue, while MLR and MKT calculations are shown in pink and light blue, respectively. The regions are filled in to show the range of values obtained using the three different chronometers, as described in Equations (12)–(14). Dashed horizontal lines indicate a value of 13.7 Gyr; solid horizontal lines indicate a value of 0 Gyr.

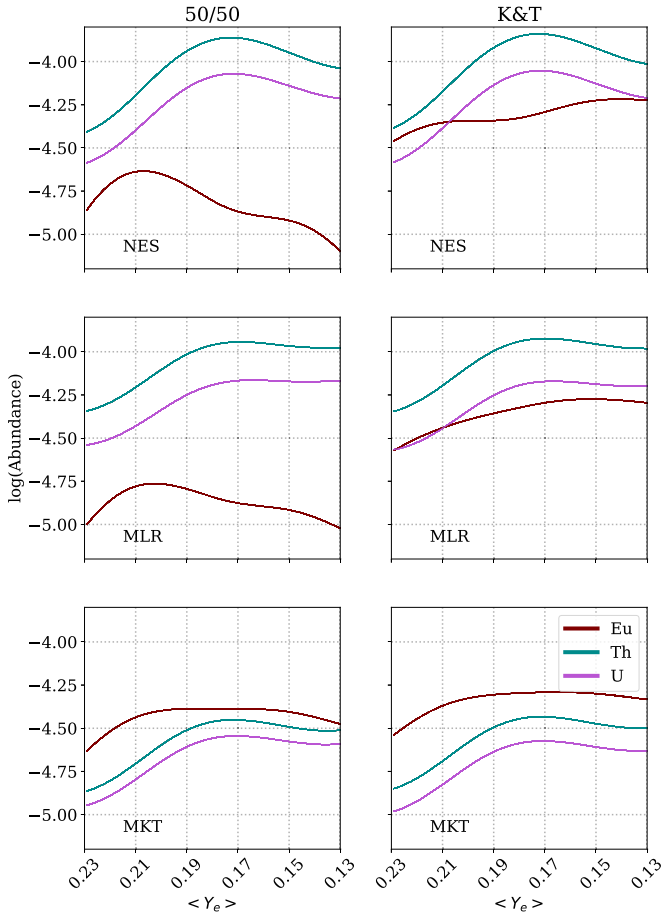


**Figure 13.** Composite values of initial production abundances of europium (red), thorium (teal), and uranium (pink), separated out by beta-decay rates used. NES, MLR, and MKT simulations are shown in the top, middle, and bottom rows, respectively. The left column shows results obtained using the 50/50 fission yields, and the right column shows those obtained using the K&T fission yields. The horizontal axis shows average $Y_e$ (with increasing neutron richness) of the combined trajectories.

this is largely overlapping age estimates stemming from the actinide chronometers, as seen in Figure 14.

In comparison, the MKT simulations yielded roughly only one-third the actinide abundances compared to MLR. However, the difference between thorium and uranium production within MKT simulations was small, as can be seen in the bottom panel of Figure 13. The overall effect of this translates into larger age estimates for MKT simulations, as shown by the light blue error bars in Figure 14 being consistently centered at larger values than the pink or dark blue. We point out, though, that the ratio is not necessarily smaller because either uranium or thorium specifically is less effectively produced. Rather both are inefficiently produced yielding overall smaller abundances.

### 4.2. Chronometric Agreement

An important assumption in Equations (12)–(14) is that of a single enrichment event, i.e., that the lanthanide and actinides observed in the *r*-process-enhanced star stem from the same event that occurred at time $t_0$. Beyond this, the chronometry equations make no other assumptions and are derived from the nuclear decay equation. Hence if the *r*-process elements in a given star come from a single event and if the abundances from

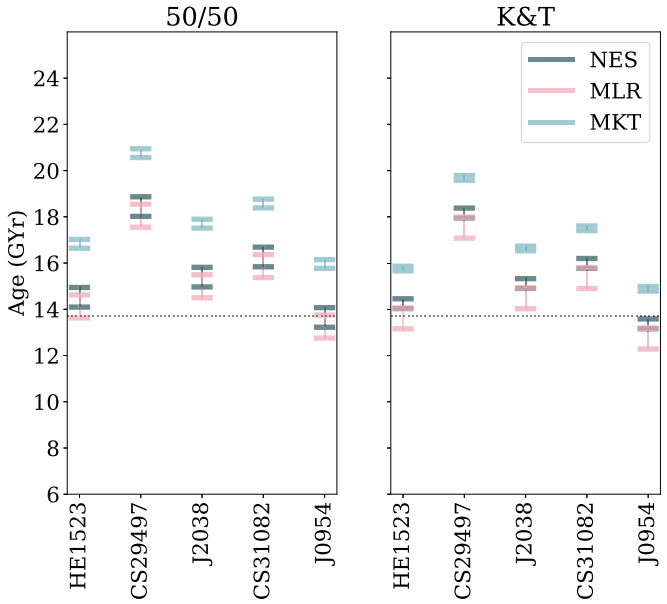


**Figure 14.** Uncertainty in age estimates due to uncertain nuclear physics and $Y_e$ for fixed stellar observations. The ages in this figure are calculated solely using the U to Th abundance. A horizontal dotted line indicates the value of 13.7 Gyr. NES, MLR, and MKT calculations are shown as dark blue, pink, and light blue bars, respectively. The left panel shows results obtained using the 50/50 fission yields while the right panel shows those obtained using the K&T fission yields.

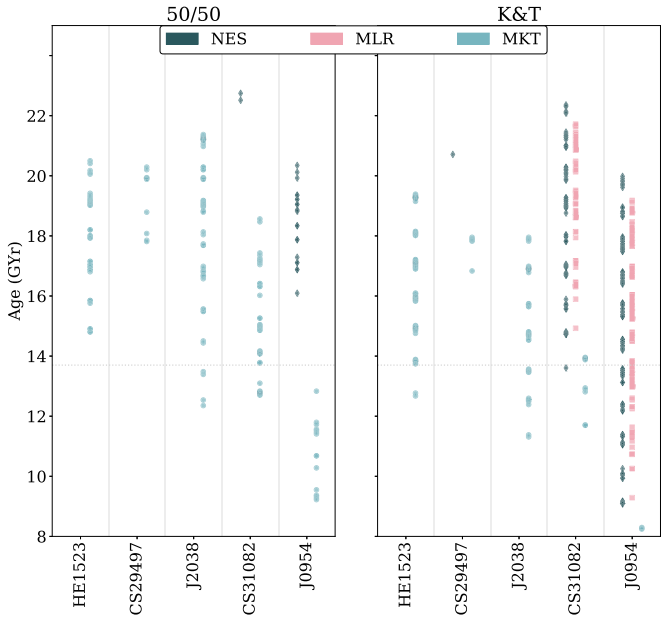


**Figure 15.** Full range of predicted age values for each star when the full range of observational error bars plus the full uncertainty from the composite trajectories are used. Each point represents an age predicted by an individual composite trajectory that shows agreement between all three chronometer pairs. Results in the left and right panels use 50/50 and K&T fission yield descriptions, respectively. NES calculations are represented as dark blue diamonds, MLR as pink squares, and MKT as light blue circles.

this event have been correctly predicted, then the three chronometers should provide the same age estimates within observational uncertainty.

With this in mind, we begin with our model set, which includes all the combinations of trajectories shown in Figure 2, each computed for all three different beta-decay rates. We then

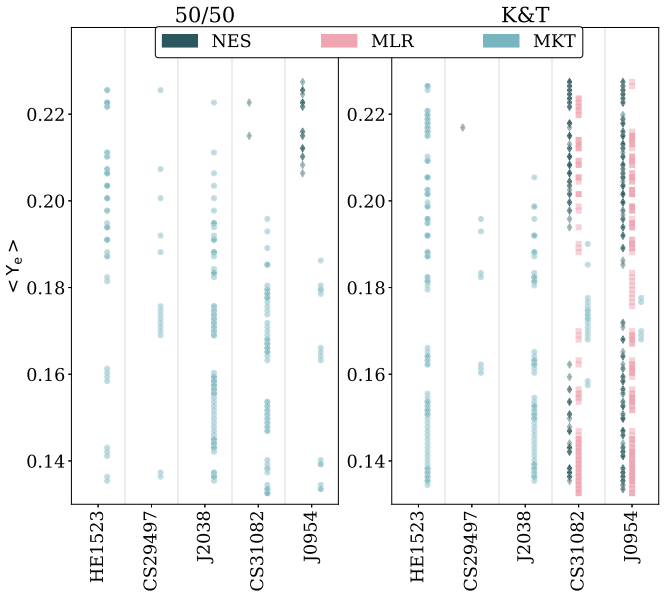


**Figure 16.** Combined trajectories (as described in Section 2, represented on the vertical axis by average $Y_e$) that yield chronometric agreement for each of the stars in our sample. The different beta-decay rates are indicated by the marker colors as in Figure 14.

select *only* those models for which each of the chronometers yield the same age within the quoted observational error bars, terming this *chronometric agreement* (or simply *agreement*). We obtain error bars from the observation by calculating the largest and smallest possible values of $\log_\epsilon(A/B)$ from the individual error bars for isotopes A and B. We show the results of this procedure in Figure 15. We see that for many stars no chronometric agreement exists for our selection of combined trajectories with the MLR and NES rates, consistent with the results of Figure 12. However we caution that all our simulations for this analysis were performed with the FRDM mass model, and this conclusion may change when a wider variety of theoretical predictions for off-stability masses are considered.

Furthermore, we have used only the combined trajectories from Figure 2, i.e., many of the extremely large values resulting from actinide–lanthanide pairs shown in Figure 12 are eliminated from our analysis. Other combinations, particularly those weighted toward even higher values of $Y_e$ (or simply more heavily weighted toward the higher-$Y_e$ range of our selection) could produce agreement for these stars.

On the other hand, for all stars, there are some simulations with the MKT rates that produce chronometric agreement, again due to their more limited production of actinides as compared to the rare Earths. For each star, the range of ages that are in agreement is larger in Figure 15 than in Figure 14. This is because we have taken into account observational uncertainty in the former.

It is interesting to see what sort of distribution of electron fraction is needed to produce the chronometric agreement. We show instances in which this occurs in Figure 16 for all three sets of beta-decay rates. As is consistent with Figure 15, we find that a very large range of the MKT calculations yields chronometric agreement when observational error bars are taken into account. In the case of the most actinide-poor star, HE1523, both high average $Y_e$ and low average $Y_e$ calculations that make use of the MKT beta-decay rates yield chronometric

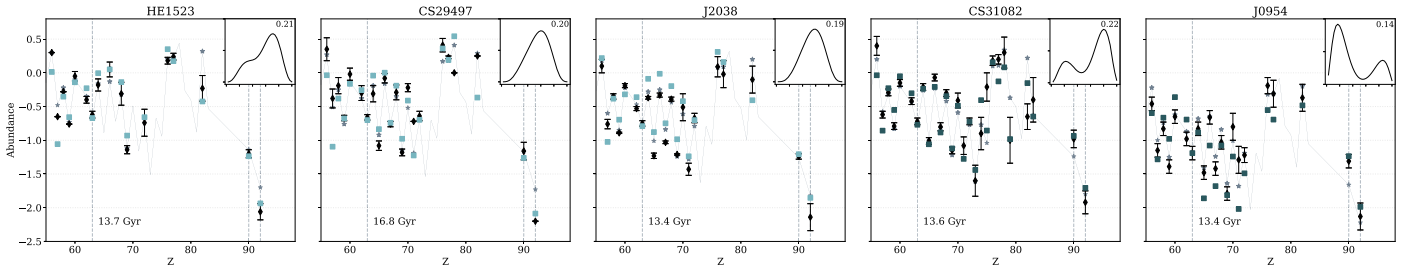


**Figure 17.** Representative theoretical abundance pattern compared to stellar and solar observations when nucleosynthesis calculations are carried out to the times indicated in each panel. The color of the squares representing the theoretical abundances indicates the set of beta-decay rates used for that particular calculation, i.e., light blue for MKT and dark blue for NES. In the upper right corner of each panel, we include the weight distribution (as could be extracted from Figure 2) used for the specific calculation for which the abundance is shown. The stellar observational values plus their error bars are shown as black diamonds, and the solar *r*-process residuals from Asplund et al. (2009) are shown as a solid gray line. We additionally show solar *r*-process abundances as gray stars when those same data points exist for the stellar observation. We highlight the elements europium ($Z = 63$), thorium ($Z = 90$), and uranium ($Z = 92$) with vertical dashed lines, as these were the elements we used to carry out our analysis. For each star, all data is scaled to europium.

agreement, independent of fission yield. Contrarily, for the stars with the largest actinide enhancement (CS31082 and J0954), the use of MKT beta-decay rates only yields agreement when the material is more heavily weighted toward mid- and/or low-$Y_e$ values.

For CS31082 and J0954, there is overlap in the NES and MLR calculations that agree when the K&T fission yields are used. This is consistent with previous work that showed agreement with K&T fission yields for J0954 using the MLR and FRDM combination as long as the average $Y_e$ was sufficiently high, and the actinides were "diluted" (Holmbeck et al. 2018b). However, if the fission daughter product distribution is taken to be 50/50, none of the MLR trajectories we have considered yield agreement, as do only a selection of NES calculations with trajectories weighted toward high $Y_e$. This is in stark contrast to the aforementioned behavior of the MKT calculations, which favor low-$Y_e$ weighted trajectories. This contrast is consistent with the abundance patterns resulting from these calculations, as seen in Figure 13. NES calculations more effectively reproduce a large actinide population, to the point of overproducing actinides. Thus only a small amount of low-$Y_e$ material is sufficient to produce a large actinide abundance.

We carry our analysis one step further by selecting instances of calculations yielding agreement from those shown in Figure 16. For each star, we select a pairing of beta-decay description and combined trajectory from those shown in Figures 15 and 16 in order to directly compare their late-time abundance pattern with both stellar and solar observations. We show the resulting abundances from each of these nucleosynthesis calculations in Figure 17. The time to which each individual set of nucleosynthesis calculations is evolved is shown in each subpanel of Figure 17. Additionally, we show the trajectory that yielded the particular abundance pattern (as well as the corresponding average $Y_e$) in the upper right corner of each panel. We find some cases of rare-Earth overproduction or underproduction. However, in general we find good agreement with the overall solar or stellar observed abundance patterns above $Z = 60$.

## 5. Conclusion

We performed a targeted study to specifically investigate the impact of global beta-decay rates on key aspects of *r*-process nucleosynthesis and KN modeling. We combined three sets of beta-decay rates with nine different mass models and two fission daughter product distributions for our nucleosynthesis calculations. Furthermore, we considered three single-$Y_e$ trajectories for the full suite of nuclear inputs in order to specifically probe the role of fission heating in our calculations. We also considered several ensembles of trajectories, meant to approximate a multicomponent ejecta, for a subset of nuclear inputs. We compared the late-time abundances for these ensembles (obtained at various times) to those from astronomical observations for five *r*-process-enhanced, metal-poor stars.

For the single $Y_e$ trajectory cases, we found a substantial difference in the predicted total heating from different mass models. The magnitude of this difference was sensitive to the value of $Y_e$, and almost entirely due to differences in the predicted alpha-decay and spontaneous fission heating. This was especially the case in trajectories with initial electron fraction at or below 0.18, as this was where a significant amount of fission or alpha decay could occur. We provided a closer investigation of some instances where the change in beta-decay rate translated to an increase of 50% or more in the bolometric luminosity averaged over 1 to 10 days, and identified key nuclei responsible for these differences. We found these increased luminosities could be attributed to both unmeasured nuclei that feed into known nuclei (such was the case for the population of, for example, $^{224}$Ra), as well as unmeasured nuclei directly responsible for heating (as was the case, for example, for several isotopes of Rf).

We found the behavior of the single-trajectory calculations was reflected in the combined trajectories using the FRDM2012 and HFB22 mass models. In these cases, the competition between alpha decay and spontaneous fission with beta decay was not as large as that in the single-trajectory cases, as all our combined trajectories had a substantial amount of material with electron fractions above 0.18. However, even in these circumstances, the description of the heating past 1 day is still incomplete without the contribution from fission and alpha decay. Furthermore, the point in time at which alpha decay and fission begin to influence the overall magnitude of the heating differs, with NES contributions becoming relevant prior to 1 day, those of MLR at approximately 1 day, and those of MKT predicting a significant contribution closer to 10 days.

Finally, we used our calculated abundances of the longest-lived isotopes of europium, thorium, and uranium to perform cosmochronometry calculations for a sample of five *r*-process-enhanced metal-poor stars. We found a larger uncertainty when we used actinide to europium ratios, as opposed to uranium to thorium ratios. This is to be expected given the larger separation between europium and the actinides in the nuclear

chart. This is consistent with the general consensus that actinide-pair chronometers are more reliable than actinide–lanthanide pairs. We do consider, however, that the actinide–lanthanide pairs can provide valuable insight, and despite the large uncertainty they contribute, we were able to draw interesting conclusions.

One conclusion is that the use of different beta-decay rates predicted disparities in the age estimated even from the actinide abundances alone. While there was significant overlap between the predictions resulting from NES and MLR actinide abundances, these differed from the MKT abundances, hinting at the extent to which these different beta-decay rates hinder or facilitate actinide production. Second, we were able to use the lanthanide abundances, together with the observational uncertainties to place a constraint on the age predictions, in the context of our model. We expand upon previous studies of chronometric dating (Holmbeck et al. 2018b, 2019; Kullmann et al. 2022) using theoretically calculated initial abundances by carefully taking into consideration the observational error bars together with multiple chronometer pairs. By doing so, we were able to find theoretically calculated abundances that yielded *chronometric agreement*, meaning that all three chronometer pairs yielded the same age. We showed that chronometric agreement depends on the beta-decay rates.

We look forward to additional experimental efforts to measure beta-decay properties (Gade & Sherrill 2016; Aprahamian et al. 2018; Tain et al. 2018; Horowitz et al. 2019; Allmond et al. 2020; Savard et al. 2020; Wu et al. 2020; Schatz et al. 2022), which will greatly help to reduce this source of uncertainty in the predictions of KN light curves and of abundance predictions. We also look forward to new theoretical predictions of the thermodynamic conditions in merging neutron stars, of fission yields and daughter products, and of neutron capture and alpha-decay rates, all of which have an important role to play.

This work was partially supported by the Fission in *r*-Process Elements (FIRE) topical collaboration in nuclear theory, funded by the U.S. DOE, contract No. DE-AC5207NA27344. This work was partially supported by the Office of Defense Nuclear Nonproliferation Research & Development (DNN R&D), National Nuclear Security Administration, US Department of Energy. This work was also possible due to support by the U.S. DOE through Los Alamos National Laboratory, operated by Triad National Security, LLC, for the National Nuclear Security Administration of the U.S. DOE. K.L. acknowledges support from the Seaborg Institute for funding under LDRD project 20210527CR, as well as from the Center for Nonlinear Studies. J.E. acknowledges support from the Nuclear Computational Low Energy Initiative (NUCLEI) SciDAC-4 project under U.S. Department of Energy grant No. DE-SC0018223 and by the U.S. We acknowledge support from the NSF (N3AS PFC) grant No. PHY-2020275, as well as from U.S. DOE contract Nos. DE-FG0202ER41216 and DE-FG0295ER40934. This research was supported in part by the National Science Foundation under grant No. PHY-1430152 (JINA Center for the Evolution of the Elements). This paper is approved for unlimited release, assigned LA-UR 22-28160.

## ORCID iDs

Kelsey A. Lund https://orcid.org/0000-0003-0031-1397
J. Engel https://orcid.org/0000-0002-2748-6640
G. C. McLaughlin https://orcid.org/0000-0001-6811-6657
M. R. Mumpower https://orcid.org/0000-0002-9950-9688
E. M. Ney https://orcid.org/0000-0001-8008-2314
R. Surman https://orcid.org/0000-0002-4729-8823

## References

Abbott, B. P., Abbott, R., Abbott, T. D., et al. 2017a, PhRvL, 119, 161101
Abbott, B. P., Abbott, R., Abbott, T. D., et al. 2017b, ApJL, 848, L12
Aboussir, Y., Pearson, J. M., Dutta, A. K., & Tondeur, F. 1995, ADNDT, 61, 127
Agathos, M., Zappa, F., Bernuzzi, S., et al. 2020, PhRvD, 101, 044006
Allmond, M., Appiah, K., Bollen, S., et al. 2020, FRIB Decay Station, https://fds.ornl.gov/wp-content/uploads/2020/09/FDS-WP.pdf
Aprahamian, A., Surman, R., Frebel, A., et al. 2018, arXiv:1809.00703
Asplund, M., Grevesse, N., Sauval, A. J., & Scott, P. 2009, ARA&A, 47, 481
Audi, G., Kondev, F. G., Wang, M., Huang, W. J., & Naimi, S. 2017, ChPhC, 41, 030001
Barnes, J., & Kasen, D. 2013, ApJ, 775, 18
Barnes, J., Kasen, D., Wu, M.-R., & Martínez-Pinedo, G. 2016, ApJ, 829, 110
Barnes, J., Zhu, Y. L., Lund, K. A., et al. 2021, ApJ, 918, 44
Bauswein, A., Goriely, S., & Janka, H. T. 2013, ApJ, 773, 78
Beun, J., McLaughlin, G. C., Surman, R., & Hix, W. R. 2008, PhRvC, 77, 035804
Burbidge, E. M., Burbidge, G. R., Fowler, W. A., & Hoyle, F. 1957, RvMP, 29, 547
Butcher, H. R. 1987, Natur, 328, 127
Caballero, O. L., Arcones, A., Borzov, I. N., Langanke, K., & Martinez-Pinedo, G. 2014, arXiv:1405.0210
Cameron, A. G. W. 1957, PASP, 69, 201
Chabanat, E., Bonche, P., & Haensel, P. 1998, NuPhA, 635, 231
Chornock, R., Berger, E., Kasen, D., et al. 2017, ApJL, 848, L19
Cowperthwaite, P. S., Berger, E., Villar, V. A., et al. 2017, ApJL, 848, L17
Díaz, M. C., Macri, L. M., Lambas, D. G., et al. 2017, ApJL, 848, L29
Duflo, J., & Zuker, A. P. 1995, PhRvC, 52, 23
Eichler, M., Arcones, A., Kelic, A., et al. 2015, ApJ, 808, 30
Eichler, M., Sayar, W., Arcones, A., & Rauscher, T. 2019, ApJ, 879, 47
Evans, P. A., Cenko, S. B., Kennea, J. A., et al. 2017, Sci, 358, 1565
Even, W., Korobkin, O., Fryer, C. L., et al. 2019, ApJ, 899, 24
Fontes, C. J., Fryer, C. L., Hungerford, A. L., Wollaeger, R. T., & Korobkin, O. 2020, MNRAS, 493, 4143
Foucart, F., Haas, R., Duez, M. D., et al. 2016, PhRvD, 93, 044019
Frebel, A., Christlieb, N., Norris, J. E., et al. 2007, ApJL, 660, L117
Gade, A., & Sherrill, B. M. 2016, PhyS, 91, 053003
Giuliani, S. A., Martínez-Pinedo, G., Wu, M. R., & Robledo, L. M. 2020, PhRvC, 102, 45804
Goriely, S. 2015, EPJA, 51, 22
Goriely, S., & Arnould, M. 2001, A&A, 379, 1113
Goriely, S., Bauswein, A., & Janka, H. T. 2011, ApJL, 738, L32
Goriely, S., Chamel, N., & Pearson, J. M. 2013, PhRvC, 88, 061302
Goriely, S., Hilaire, S., Koning, A. J., Sin, M., & Capote, R. 2009, PhRvC, 79, 024612
Grossman, D., Korobkin, O., Rosswog, S., & Piran, T. 2014, MNRAS, 439, 757
Hill, V., Christlieb, N., Beers, T. C., et al. 2017, A&A, 607, A91
Hill, V., Plez, B., Cayrel, R., et al. 2002, A&A, 387, 560
Holmbeck, E. M., Beers, T. C., Roederer, I. U., et al. 2018a, ApJL, 859, L24
Holmbeck, E. M., Frebel, A., McLaughlin, G. C., et al. 2019, ApJ, 881, 5
Holmbeck, E. M., Sprouse, T. M., Mumpower, M. R., et al. 2018b, ApJ, 870, 23
Horowitz, C. J., Arcones, A., Côté, B., et al. 2019, JPhG, 46, 083001
Hotokezaka, K., Kiuchi, K., Kyutoku, K., et al. 2013, PhRvD, 87, 024001
Just, O., Bauswein, A., Pulpillo, R. A., Goriely, S., & Janka, H.-T. 2015, MNRAS, 448, 541
Karpov, A. V., Zagrebaev, V. I., Martinez Palenzuela, Y., Felipe Ruiz, L., & Greiner, W. 2012, IJMPE, 21, 1250013
Kasen, D., Badnell, N. R., & Barnes, J. 2013, ApJ, 774, 25
Kasen, D., & Barnes, J. 2019, ApJ, 876, 128
Kasen, D., Metzger, B., Barnes, J., Quataert, E., & Ramirez-Ruiz, E. 2017, Natur, 551, 80
Kashyap, R., Das, A., Radice, D., et al. 2022, PhRvD, 105, 103022
Kawano, T., Capote, R., Hilaire, S., & Chau Huu-Tai, P. 2016, PhRvC, 94, 014612

Kodama, T., & Takahashi, K. 1975, NuPhA, 239, 489
Korobkin, O., Rosswog, S., Arcones, A., & Winteler, C. 2012, MNRAS, 426, 1940
Kortelainen, M., McDonnell, J., Nazarewicz, W., et al. 2012, PhRvC, 85, 024304
Kullmann, I., Goriely, S., Just, O., et al. 2021, MNRAS, 510, 2804
Kullmann, I., Goriely, S., Just, O., Bauswein, A., & Janka, H. T. 2022, arXiv:2207.07421
Lattimer, J. M., & Schramm, D. N. 1974, ApJL, 192, L145
Lattimer, J. M., & Schramm, D. N. 1976, ApJ, 210, 549
Lehner, L., Liebling, S. L., Palenzuela, C., et al. 2016, CQGra, 33, 184002
Li, L.-X., & Paczyński, B. 1998, ApJL, 507, L59
Li, X., & Siegel, D. M. 2021, PhRvL, 126, 251101
Liu, M., Wang, N., Deng, Y., & Wu, X. 2011, PhRvC, 84, 014333
Malkus, A., Kneller, J. P., McLaughlin, G. C., & Surman, R. 2012, PhRvD, 86, 085015
Mamdouh, A., Pearson, J. M., Rayet, M., & Tondeur, F. 2001, NuPhA, 679, 337
Marketin, T., Huther, L., & Martínez-Pinedo, G. 2016, PhRvC, 93, 025805
Martin, D., Perego, A., Arcones, A., et al. 2015, ApJ, 813, 2
Martin, D., Perego, A., Kastaun, W., & Arcones, A. 2018, CQGra, 35, 034001
Mendoza-Temis, J. d. J., Wu, M.-R., Langanke, K., et al. 2015, PhRvC, 92, 055805
Metzger, B. D. 2020, LRR, 23, 1
Metzger, B. D., Martínez-Pinedo, G., Darbha, S., et al. 2010, MNRAS, 406, 2650
Miller, J. M., Ryan, B. R., Dolence, J. C., et al. 2019, PhRvD, 100, 23008
Möller, P., Mumpower, M. R., Kawano, T., & Myers, W. D. 2019, ADNDT, 125, 1
Möller, P., Pfeiffer, B., & Kratz, K.-L. 2003, PhRvC, 67, 055802
Möller, P., Sierk, A. J., Ichikawa, T., Iwamoto, A., & Mumpower, M. 2015, PhRvC, 91, 024310
Möller, P., Sierk, A. J., Ichikawa, T., & Sagawa, H. 2016, ADNDT, 109, 1
Mumpower, M. R., Kawano, T., & Möller, P. 2016a, PhRvC, 94, 064317
Mumpower, M. R., Kawano, T., Sprouse, T. M., et al. 2018, ApJ, 869, 14
Mumpower, M. R., Surman, R., McLaughlin, G. C., & Aprahamian, A. 2016b, PrPNP, 86, 86
Mustonen, M. T., & Engel, J. 2016, PhRvC, 93, 014304
Myers, W. D., & Świątecki, W. J. 1996, NuPhA, 601, 141
Myers, W. D., & Świątecki, W. J. 1999, PhRvC, 60, 014606
Nedora, V., Bernuzzi, S., Radice, D., et al. 2021, ApJ, 906, 98
Ney, E. M., Engel, J., Li, T., & Schunck, N. 2020, PhRvC, 102, 1
Nicholl, M., Berger, E., Kasen, D., et al. 2017, ApJL, 848, L18
Nikas, S., Perdikakis, G., Beard, M., et al. 2020, arXiv:2010.01698
Oechslin, R., Janka, H.-T., & Marek, A. 2007, A&A, 467, 395
Orford, R., Vassh, N., Clark, J. A., et al. 2022, PhRvC, 105, L052802
Panov, I. V., & Janka, H. T. 2009, A&A, 494, 829
Perego, A., Radice, D., & Bernuzzi, S. 2017, ApJL, 850, L37
Placco, V. M., Holmbeck, E. M., Frebel, A., et al. 2017, ApJ, 844, 18
Radice, D., Galeazzi, F., Lippuner, J., et al. 2016, MNRAS, 460, 3255
Radice, D., Perego, A., Hotokezaka, K., et al. 2018, ApJ, 869, 130
Ren, J., Christlieb, N., & Zhao, G. 2012, A&A, 537, A118
Ristic, M., Holmbeck, E. M., Wollaeger, R., et al. 2022, arXiv:2206.02273
Roberts, L. F., Kasen, D., Lee, W. H., & Ramirez-Ruiz, E. 2011, ApJL, 736, L21
Robin, C., Litvinova, E., & Martínez-Pinedo, G. 2022, in EPJ Web Conf. 260, The 16th International Symp. on Nuclei in the Cosmos (NIC-XVI) (Les Ulis: EDP Sciences), 03002
Rosswog, S., Liebenörfer, M., Thielemann, F., et al. 1999, A&A, 341, 499
Ruffert, M., Janka, H. T., Takahashi, K., & Schäfer, G. 1997, A&A, 319, 122
Savard, G., Brodeur, M., Clark, J. A., Knaack, R. A., & Valverde, A. A. 2020, NIMPB, 463, 258
Schatz, H., Becerril Reyes, A. D., Best, A., et al. 2022, JPhG, 49, 110502
Schatz, H., Toenjes, R., Pfeiffer, B., et al. 2002, ApJ, 579, 626
Sekiguchi, Y., Kiuchi, K., Kyutoku, K., & Shibata, M. 2015, PhRvD, 91, 064059
Shafer, T., Engel, J., Fröhlich, C., et al. 2016, PhRvC, 94, 055802
Shibata, M., Taniguchi, K., & Uryū, K. b. 2005, PhRvD, 71, 084021
Siegel, D. M., & Metzger, B. D. 2017, PhRvL, 119, 231102
Siqueira Mello, C., Spite, M., Barbuy, B., et al. 2013, A&A, 550, A122
Sprouse, T. M., Navarro Perez, R., Surman, R., et al. 2020, PhRvC, 101, 055803
Steiner, A. W., Hempel, M., & Fischer, T. 2013, ApJ, 774, 17
Stewart, A. R., Lo, L.-T., Korobkin, O., et al. 2022, arXiv:2201.01865
Tain, J. L., Agramunt, J., Ahn, D. S., et al. 2018, AcPPB, 49, 417
Tanaka, M., & Hotokezaka, K. 2013, ApJ, 775, 113
Tanaka, M., Kato, D., Gaigalas, G., & Kawaguchi, K. 2020, MNRAS, 496, 1369
Vassh, N., Vogt, R., Surman, R., et al. 2019, JPhG, 46, 065202
Virtanen, P., Gommers, R., Oliphant, T. E., et al. 2020, NatMe, 17, 261
Wanajo, S., Sekiguchi, Y., Nishimura, N., et al. 2014, ApJL, 789, L39
Wang, M., Audi, G., Kondev, F. G., et al. 2017, ChPhC, 41, 030003
Wollaeger, R. T., Korobkin, O., Fontes, C. J., et al. 2018, MNRAS, 478, 3298
Wu, J., Nishimura, S., Möller, P., et al. 2020, PhRvC, 101, 042801
Wu, M.-R., Barnes, J., Martínez-Pinedo, G., & Metzger, B. D. 2019, PhRvL, 122, 62701
Zagrebaev, V. I., Karpov, A. V., Mishustin, I. N., & Greiner, W. 2011, PhRvC, 84, 044617
Zhu, Y., Wollaeger, R. T., Vassh, N., et al. 2018, ApJL, 863, L23
Zhu, Y. L., Lund, K. A., Barnes, J., et al. 2021, ApJ, 906, 94